


## The Intrinsic Sizes of Odd Radio Circles

DAVID S. N. RUPKE <sup>1,2</sup> ALISON L. COIL <sup>3</sup> KELLY E. WHALEN <sup>4,5</sup> JOHN MOUSTAKAS <sup>6</sup>,  
CHRISTY A. TREMONTI <sup>7</sup> AND SERENA PERROTTA <sup>3</sup>

<sup>1</sup>*Department of Physics, Rhodes College, 2000 North Parkway, Memphis, TN 38112, USA*

<sup>2</sup>*Zentrum für Astronomie der Universität Heidelberg, Astronomisches Rechen-Institut, Mönchhofstr 12-14, D-69120 Heidelberg, Germany*

<sup>3</sup>*Department of Astronomy and Astrophysics, University of California, San Diego, La Jolla, CA 92093, USA*

<sup>4</sup>*Department of Physics and Astronomy, Dartmouth College, Hanover, NH 03755, USA*

<sup>5</sup>*Goddard Space Flight Center, Greenbelt, MD*

<sup>6</sup>*Department of Physics and Astronomy, Siena College, Loudonville, NY 12211, USA*

<sup>7</sup>*Department of Astronomy, University of Wisconsin-Madison, Madison, WI 53706, USA*

(Received 11 Dec 2023; Revised 21 Mar 2024; Accepted 29 Mar 2024)

Submitted to ApJ

### ABSTRACT

A new class of radio source, the so-called Odd Radio Circles (ORCs), have been discovered by recent sensitive, large-area radio continuum surveys. The distances of these sources have so far relied on photometric redshifts of optical galaxies found at the centers of or near the ORCs. Here we present Gemini rest-frame optical spectroscopy of six galaxies at the centers of, or potentially associated with, the first five ORC discoveries. We supplement this with Legacy Survey imaging and Prospector fits to their *griz*+*W1*/*W2* photometry. Of the three ORCs with central galaxies, all lie at distances ( $z = 0.27 - 0.55$ ) that confirm the large intrinsic diameters of the radio circles (300–500 kpc). The central galaxies are massive ( $M_* \sim 10^{11} M_\odot$ ), red, unobscured ellipticals with old ( $\gtrsim 1$  Gyr) stellar populations. They have LINER spectral types that are shock- or AGN-powered. All three host low-luminosity, radio-quiet AGN. The similarity of their central galaxies are consistent with a common origin, perhaps as a blastwave from an ancient starburst. The other two ORCs are adjacent and have no prominent central galaxies. However, the  $z = 0.25$  disk galaxy that lies between them hosts a Type 2, moderate-luminosity AGN. They may instead be the lobes of a radio jet from this AGN.

### 1. INTRODUCTION

The Odd Radio Circles (ORCs) are a new class of radio source (Norris et al. 2021b). ORCs are large rings of faint, diffuse continuum emission spanning  $\sim 1$  arcminute. The first examples of this class were detected at 1 GHz in the Evolutionary Map of the Universe (EMU; Norris et al. 2011) Pilot Survey (Hotan et al. 2021) using the Australian Square Kilometer Array Pathfinder (ASKAP). The EMU Pilot Survey is able to find rare, faint objects because it achieves  $\sim 12''$  resolution; is sensitive to low surface brightness emission, reaching  $\sim 30 \mu\text{Jy beam}^{-1}$ ; and covers  $270 \text{ deg}^2$  of the sky.

Several other ORCs, or ORC-like structures, have subsequently been discovered. Norris et al. (2021b) present ORC4 alongside ORCs 1–3 after finding it in reprocessed 325 MHz Giant MeterWave Radio Telescope (GMRT) data (Venturi et al. 2017; Intema et al. 2017). Koribalski et al. (2021) discovered ORC J0102–2450 (labeled ORC5 by Norris et al. 2021a) in later ASKAP data. Inspired by previous detections, Omar (2022) describe an ORC in Low Frequency Array (LOFAR) survey data. Filipović et al. (2022) show an exceptionally large example, J0624–6948, observed with ASKAP. Gupta et al. (2022) deliver two ORC “candidates” and Lochner et al. (2023) describe an ORC-like structure; all three were found using machine learning techniques applied to low-frequency survey data (ASKAP and MeerKAT).

Nine of these ten structures are probably extragalactic in origin. The most likely Galactic origin of ORCs, that of a disk supernova remnant, is largely ruled out

by the high Galactic latitudes of most ORCs or ORC candidates:  $|b| \gtrsim 20^\circ$  (Norris et al. 2021b; Sarbadhicary et al. 2022). The exception is J0624–6948, which is  $3^\circ$  from the radio edge of the Large Magellanic Cloud. Circumgalactic or intragroup supernova remnants are also possible but unlikely for the other ORCs (Sarbadhicary et al. 2022; Norris et al. 2022)

The remaining nine sources consist of large, limb-brightened circular objects that often have clumpy substructure in the rings. Many also contain irregular interior emission. At least 5/9 have a galaxy at or near the geometric center of the ORC with a photometric redshift in the range  $z = 0.27 - 0.56$ : ORCs 1, 4, and 5 (Norris et al. 2022); EMU-PS J222339.5–483449 (Gupta et al. 2022); and the so-called SAURON object (Lochner et al. 2023). Adopting these redshifts, the intrinsic sizes of the ORCs are several hundred kpc in diameter.

The physical mechanism that produces such enormous radio structures is yet unknown. Candidates include a blast wave from an explosive event due to star formation or active galactic nuclei (Norris et al. 2022; Coil et al. 2024), a shockwave from an extreme galaxy merger (Dolag et al. 2023), or a galaxy virial shock (Yamasaki et al. 2024).

Higher-resolution, multi-band radio measurements of ORC1 are consistent with the blastwave scenario (Norris et al. 2022). In Coil et al. (2024), we advance further evidence in favor of this model through deep, rest-frame, near-UV/optical integral field spectroscopy of ORC4 with the Keck Cosmic Web Imager (KCWI). These KCWI data constrain the redshift of the central source to  $z = 0.4512$  and reveal strong [O II] 3727, 3729 Å ionized gas emission. This emission extends to 20 kpc radius, shows a velocity gradient and high velocity dispersion (150–200 km s<sup>−1</sup>), and has very high equivalent width (50 Å). Photometry of the  $10^{11} M_\odot$  central galaxy is consistent with a 1 Gyr-old burst of star formation that formed half of the galaxy’s stars. Accompanying numerical simulations suggest that this burst could have produced the large-scale radio emission through a forward shock driven by a powerful wind. The  $10\times$  smaller ionized gas emission is the result of gas heated by the reverse shock that then falls back towards the central galaxy and produces further, small-scale shocks.

To explore the nature of the central galaxies of ORCs, we here present new rest-frame optical spectroscopy ( $\sim 3700$  to  $6800$  Å) of the central galaxies of ORCs 1, 4, and 5. We also target several galaxies near these central galaxies. For ORCs 2/3, which are spatially adjacent but do not contain prominent central galaxies, we target a bright galaxy located in projection between their centers. We also analyze deep photometry from the

**Table 1.** Observations

Target	Instrument	Date	$t_{\text{exp}}$	$\lambda_{\text{cen}}$	PA
			s	nm	°
(1)	(2)	(3)	(4)	(5)	(6)
ORC1	GMOS-S	30 Aug 2022	941×3	705/750/795	83.8
ORC2/3	GMOS-S	19 Jun 2022	940×3	705/750/795	270.0
ORC4	GMOS-N	5 Jun 2022	704×4	710/714	153.0
ORC5	GMOS-S	11 Jun 2022	941×3	705/750/795	315.8

NOTE—Column 1: Science target. Column 2: Instrument. Column 3: UTC observation date. Column 4: Exposure time, in s. Column 5: Central wavelength of grating tilt, in nm. Column 6: Sky position angle of slit, in degrees East of North.

Dark Energy Spectroscopic Instrument (DESI) Legacy Surveys to constrain the masses and star formation history of the associated galaxies.

In Section 2, we present the spectroscopic observations and data reduction, multicolor images of the ORC fields, and the Tractor photometry. In Section 3, we present the resulting spectra, fits to the spectra and photometry, and the resulting physical quantities derived from these fits. We discuss the properties of the galaxies in light of these data, as well as the implications for the origin of ORCs, in Section 4. We conclude in Section 5. In all calculations, we assume a flat  $\Lambda$  cosmology with  $\Omega_m = 0.315$  and  $H_0 = 67.4$  km s<sup>−1</sup> Mpc<sup>−1</sup>. In our star formation rate (SFR) calculations, we assume a Salpeter IMF.

## 2. OBSERVATIONS AND DATA REDUCTION

### 2.1. Spectroscopy

We observed ORCs 1–5 with the Gemini Multi-Object Spectrographs on Gemini North and South (GMOS-N and GMOS-S; Hook et al. 2004; Gimeno et al. 2016). In designing the observations, we specified observing conditions of 70th-percentile image quality (IQ70) and 50th-percentile cloud cover (CC50). The actual observations are summarized in Table 1. We used the R400 grating with a  $0''.75$  slit to achieve a spectral resolution of  $\delta\lambda = 4.0$  Å. The GG455 filter reduces second-order contamination. We binned  $2\times 2$  to increase sensitivity. To minimize the effects of detector artifacts and span chip gaps, we dithered in wavelength. We especially needed

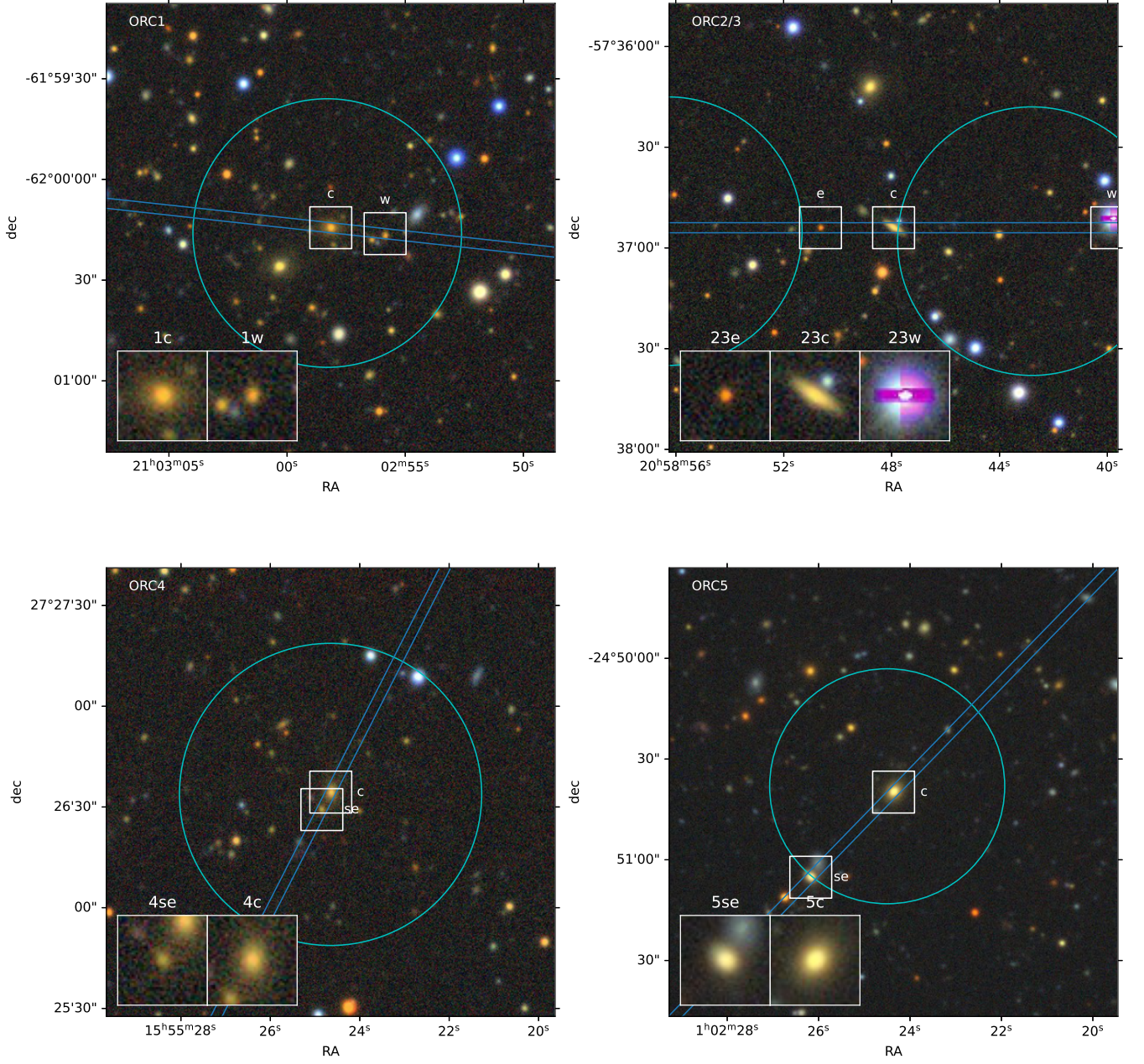


**Figure 1.** DESI Legacy Imaging Survey DR10 *griz* color images of the target fields. Sizes are approximately  $2' \times 2'$ , which is roughly double the diameter of the ORCs (Norris et al. 2021b; Koribalski et al. 2021). Cyan circles represent the ORC extents, with centers from Norris et al. (2021b) and Koribalski et al. (2021) and diameters from Norris et al. (2022). Slits are overlaid, enlarged in width for presentation. Extracted sources are labeled with boxes, and zoomed-in cutouts are in the lower left of each panel.



**Table 2.** Coordinates and Morphology

Label	RA	dec	TYPE	$n$	$R_e$	$f_{p/s}$
	hms	dms			"	
(1)	(2)	(3)	(4)	(5)	(6)	(7)
ORC1c	21:02:58.15 $\pm$ 0.12	-62:00:14.404 $\pm$ 0.004	SER	6.0	3.52	4.05
ORC23c	20:58:47.92 $\pm$ 0.08	-57:36:53.944 $\pm$ 0.002	EXP	1.0	1.69	1.96
ORC4c	15:55:24.64 $\pm$ 0.09	+27:26:34.311 $\pm$ 0.007	DEV	4.0	2.76	3.50
ORC4se	15:55:24.85 $\pm$ 0.23	+27:26:29.230 $\pm$ 0.016	DEV	4.0	0.55	1.85
ORC5c	01:02:24.35 $\pm$ 0.08	-24:50:39.736 $\pm$ 0.004	SER	5.4	1.07	1.69
ORC5se	01:02:26.17 $\pm$ 0.80	-24:51:05.100 $\pm$ 0.025	SER	3.3	0.86	1.98
ORC1w	21:02:55.85 $\pm$ 0.20	-62:00:16.799 $\pm$ 0.008	DEV	4.0	0.44	3.85
ORC23e	20:58:50.62 $\pm$ 0.14	-57:36:54.033 $\pm$ 0.005	PSF	...	...	1.12
ORC23w	20:58:39.79 $\pm$ 0.00	-57:36:51.256 $\pm$ 0.000	PSF	...	...	142.40 <sup>a</sup>

NOTE—Column 1: Label from Figure 1. Columns 2–3: Coordinates from DESI Legacy Imaging Surveys. Column 4: The fitted morphological type (PSF = point source/star; SER = Sérsic profile; EXP = exponential profile (spiral galaxy); and DEV = deVaucoulers profile (elliptical galaxy). Column 5: Sérsic index. Fixed for EXP or DEV types; allowed to vary for SER. Column 6: Half-light (effective) radius, in arcseconds. Column 7: Average ratio in  $r$  and  $i$  bands between DESI photometry and synthetic photometry from spectra.

<sup>a</sup>This value is unusually high because the slit only grazes the star's point spread function.

**Table 3.** Photometry

Label	$g$	$r$	$i$	$z$	W1	W2	W3	W4
(1)	(2)	(3)	(4)	(5)	(6)	(7)	(8)	(9)
ORC1c	21.485 <sup>+0.031</sup> <sub>-0.030</sub>	19.544 <sup>+0.006</sup> <sub>-0.006</sub>	18.668 <sup>+0.007</sup> <sub>-0.007</sub>	18.221 <sup>+0.007</sup> <sub>-0.007</sub>	17.234 <sup>+0.008</sup> <sub>-0.008</sub>	17.710 <sup>+0.023</sup> <sub>-0.022</sub>	>17.467	>14.248
ORC23c	20.761 <sup>+0.008</sup> <sub>-0.008</sub>	19.473 <sup>+0.004</sup> <sub>-0.004</sub>	18.946 <sup>+0.005</sup> <sub>-0.005</sub>	18.629 <sup>+0.004</sup> <sub>-0.004</sub>	18.139 <sup>+0.012</sup> <sub>-0.012</sub>	18.277 <sup>+0.028</sup> <sub>-0.027</sub>	16.735 <sup>+0.190</sup> <sub>-0.162</sub>	>14.424
ORC4c	21.028 <sup>+0.019</sup> <sub>-0.018</sub>	19.524 <sup>+0.007</sup> <sub>-0.007</sub>	18.910 <sup>+0.008</sup> <sub>-0.008</sub>	18.537 <sup>+0.010</sup> <sub>-0.010</sub>	17.891 <sup>+0.012</sup> <sub>-0.011</sub>	18.372 <sup>+0.035</sup> <sub>-0.033</sub>	>17.922	>14.893
ORC4se	23.559 <sup>+0.095</sup> <sub>-0.087</sub>	21.809 <sup>+0.027</sup> <sub>-0.026</sub>	21.082 <sup>+0.027</sup> <sub>-0.027</sub>	20.786 <sup>+0.038</sup> <sub>-0.037</sub>	20.241 <sup>+0.070</sup> <sub>-0.066</sub>	20.682 <sup>+0.235</sup> <sub>-0.193</sub>	>18.156	>15.019
ORC5c	20.247 <sup>+0.005</sup> <sub>-0.005</sub>	18.788 <sup>+0.002</sup> <sub>-0.002</sub>	18.309 <sup>+0.001</sup> <sub>-0.001</sub>	18.032 <sup>+0.001</sup> <sub>-0.001</sub>	17.894 <sup>+0.010</sup> <sub>-0.010</sub>	18.344 <sup>+0.031</sup> <sub>-0.030</sub>	>17.401	14.077 <sup>+0.335</sup> <sub>-0.256</sub>
ORC5se	20.355 <sup>+0.004</sup> <sub>-0.004</sub>	19.338 <sup>+0.003</sup> <sub>-0.003</sub>	18.806 <sup>+0.001</sup> <sub>-0.001</sub>	18.564 <sup>+0.002</sup> <sub>-0.002</sub>	18.175 <sup>+0.013</sup> <sub>-0.013</sub>	18.159 <sup>+0.026</sup> <sub>-0.026</sub>	16.382 <sup>+0.148</sup> <sub>-0.130</sub>	>14.357
ORC1w	23.518 <sup>+0.085</sup> <sub>-0.079</sub>	21.601 <sup>+0.014</sup> <sub>-0.014</sub>	20.770 <sup>+0.024</sup> <sub>-0.024</sub>	20.335 <sup>+0.017</sup> <sub>-0.017</sub>	19.138 <sup>+0.027</sup> <sub>-0.026</sub>	19.773 <sup>+0.100</sup> <sub>-0.092</sub>	>17.801	>14.442
ORC23e	24.350 <sup>+0.115</sup> <sub>-0.104</sub>	22.704 <sup>+0.036</sup> <sub>-0.035</sub>	21.128 <sup>+0.019</sup> <sub>-0.018</sub>	20.476 <sup>+0.012</sup> <sub>-0.012</sub>	20.657 <sup>+0.096</sup> <sub>-0.088</sub>	>21.263	>17.590	>14.465
ORC23w	15.073 <sup>+0.000</sup> <sub>-0.000</sub>	14.717 <sup>+0.001</sup> <sub>-0.001</sub>	14.583 <sup>+0.001</sup> <sub>-0.001</sub>	14.588 <sup>+0.000</sup> <sub>-0.000</sub>	16.031 <sup>+0.003</sup> <sub>-0.003</sub>	16.712 <sup>+0.008</sup> <sub>-0.008</sub>	>17.593	>14.450

NOTE—Column 1: Label from Figure 1. Columns 2–9: Tractor (Lang et al. 2016a,b) photometry from DESI Legacy Surveys (Dey et al. 2019). Magnitudes are AB and calculated directly from the catalog flux in nanomaggies using  $m = 22.5 - 2.5 \log_{10}(\text{flux})$ . We have also corrected each flux for Galactic extinction by dividing by MW\_TRANSMISSION from the Legacy Survey catalog. We require  $3\sigma$  detections, and otherwise list  $3\sigma$  lower limits in AB mags.

to mitigate the bad amplifier 5 of CCD2 on GMOS-S, but also some enhanced noise elsewhere in the GMOS-S detector and a hot column in amplifier 5 of GMOS-N. We also dithered along the slit by  $\pm 1''$ . The resulting observed wavelength ranges are 4770–9560 Å and 4730–10340 Å for GMOS-N and GMOS-S, respectively.

In Figure 1 we show images of the ORC fields (see Section 2.2). For ORCs 1, 4, and 5, we chose the slit position and PA to cover the galaxy at the center of the ORC and one other source within the ORC footprint. Following the lead of Norris et al. (2022), we denote the central sources as ORC1c, ORC4c, and ORC5c. For ORCs 2+3, we centered the slit on the galaxy directly between the two ORCs (also called ORC2/3c) and chose a PA crossing the center of each ORC.

We observed the flux standards BD+28 4211 and LTT 7379 for calibration of the GMOS-N and -S data, respectively. For the GMOS-N data, the flux standard was observed only at central wavelengths 705 and 795 nm. For GMOS-S, the standard was observed at the mean of the central wavelengths, 712 nm. However, second-order contamination is a problem above 9000 Å for the GMOS-N standard. We found in the Gemini Observatory Archive data of EG 131 taken in 2022 Sep. with the same configuration as BD+28 4211, except using the RG610 filter. We applied the resulting sensitivity function from this standard above 9000 Å, but used the original sensitivity function for lower wavelengths.

We reduced the data using v1.11 and v1.12 of `PyPeIt` (Prochaska et al. 2020). We retrieved from the Gemini Observatory Archive individual bias frames taken within a few days of each set of observations for bias subtraction. By studying the GCAL flats, we observed changes in the positions of bad/unexposed areas of the detector (bad columns, amplifiers, or slit gaps) compared to those specified by the default bad pixel masks (bpms) in `PyPeIt`. This includes changes in the slit gaps in GMOS-S between the June and August observations when a detector repair was attempted. To account for this, we edited by hand the default bpm for each configuration. We also encountered large RMS values when applying the default wavelength calibrations to the observed CuAr lamp exposures. To mitigate this, we ran `pypeit_identify` with a curated linelist on one of the extracted spectra in each wavelength configuration. `PyPeIt` also converts to vacuum wavelengths and corrects to heliocentric velocity.

During flux calibration, we used the IR algorithm for computing the sensitivity function. We corrected the data for airmass differences with the flux standards where necessary. We did not, however, apply slit loss corrections arising from not observing at the parallactic

angle. For our data, we estimate these wavelength-dependent losses to be small ( $\lesssim 10\%$  correction at the edges of the data<sup>1</sup>) because either the difference from parallactic was  $< 20^\circ$  and/or the airmass was  $\leq 1.2$  and because the target was acquired in the  $r$  band. We also applied a correction for Galactic extinction to each spectrum (Schlafly & Finkbeiner 2011).

## 2.2. Images

We retrieve coordinates and morphology (Table 2), photometry (Table 3), and *griz* images (Figure 1) from Data Release 10.1 of the DESI Legacy Imaging Surveys (Dey et al. 2019). The shape information and photometry are derived from Tractor<sup>2</sup> (Lang et al. 2016a,b) models of each source. For further details on the imaging and shape modeling, see Moustakas et al. (2023). To verify our spectrophotometry, we create synthetic  $r$  and  $i$  fluxes with `pyphot` (Fouesneau 2022) and the DESI Imaging Survey (*grz*) and DECam DR1 (*i*) response curves tabulated in `speclite`<sup>3</sup>. The average ratio between the Tractor fluxes (corrected for Galactic extinction) and our synthetic photometry are listed in Table 2 as  $f_{p/s}$ . For the small M-dwarf covered completely by one of our slits (ORC23e), this ratio is close to unity. (The other star is only barely in the slit, resulting in  $f_{p/s} > 100$ .) For the other 7 sources that are spatially-resolved in imaging, this ratio ranges from 1.7–4. We attribute this mainly to slit losses. This is borne out by the fact that the four sources with modeled half-light radius  $R_e < 2''$  have  $f_{p/s} = 1.7 - 2.0$ , while the larger sources have  $f_{p/s} = 3.5 - 4.1$ . (ORC1w does not fit this pattern because it does not fall completely in the slit). However, we also caution that the Tractor photometry is based on images taken in seeing sometimes as large as  $\text{FWHM} \sim 1.7''$ . KCWI  $g$ -band integral field data of ORC4c give  $R_e = 0.8''$  (Coil et al. 2024), and the flux ratio of the KCWI-to-GMOS spectra over identical wavelength ranges is  $\sim 1.5$ . This compares to  $R_e = 2.8''$  and  $f_{p/s} = 3.5$  from the Tractor catalog.

Regardless of the normalization, the shape of the source SEDs from Tractor photometry match well with our spectrophotometry. This is apparent visually in the overlap of the (scaled) photometry with our spectra in Figures 2–6.

## 3. RESULTS AND MODELING

### 3.1. Spectra

<sup>1</sup> <https://www.gemini.edu/observing/resources/optical-resources#ADR>

<sup>2</sup> <https://github.com/dstndstn/tractor>

<sup>3</sup> <https://speclite.readthedocs.org>

We extracted nine spectra from the four fields based on their continuum traces. We visually inspected the sky-subtracted 2D data for extended line emission along the slit, but none was apparent. Six of these are galaxies for which we determined redshifts and other properties from spectral fits (Figure 2). For three others (Figure 6 in Appendix 6), two are likely stars (ORC23e and ORC23w). The spectrum of ORC23e resembles an M-dwarf, and ORC23w a hotter, bluer star. The photometry confirms this, as we discuss above. The final spectrum, of ORC1w, is low signal-to-noise in part because the object did not fully fall in the slit; we do not identify the source.

We fit the spectra of galaxies with identifiable redshifts using IFSFIT (Rupke 2014; Rupke et al. 2017). IFSFIT first masks emission lines; fits a continuum model; and then fits the resulting continuum-subtracted emission-line spectrum. We use `ppxf` (Cappellari 2012, 2017) to fit the stellar continua using the C3K theoretical stellar libraries at solar metallicity (Choi et al. 2016; Byrne & Stanway 2023). We allow for stellar attenuation in `ppxf`. We also include an additive Legendre polynomial of order 7 with positive-definite coefficients to account for small errors in flux calibration and/or slit losses. We estimate errors in the stellar fit parameters by refitting Monte Carlo realizations of the data. We fit emission lines with a single component and require a  $2.5\sigma$  detection in  $H\alpha$  and/or  $[O II]$  3727, 3729 Å. We estimate emission-line errors from the covariance matrix. Table 4 lists the stellar and gas redshifts and velocity dispersions we measure from the fits, as well as the stellar color excess. We estimate an inferred black hole mass from  $\sigma_*$  using the McConnell & Ma (2013) prescription and also list this in Table 4.

For visual inspection of the results of these fits, Figure 3 shows close-up views of the regions around select emission lines.

To parameterize the stellar ages, we quantify the percentage contribution to the total starlight model at a rest-frame wavelength of 5000 Å in bins of young (<100 Myr), intermediate-age (100 Myr – 1 Gyr), and old (>1 Gyr) populations from the stellar libraries used to model the continuum. These percentages are listed in Table 4. (The sum may be less than 100% if there is an additive polynomial contribution.) We also calculate the  $D_n(4000)$  index to parameterize the Balmer break (Balogh et al. 1999), which monotonically increases with the age after an instantaneous burst (Kauffmann et al. 2003a).

For spectra in which  $H\beta$  is detected at  $2\sigma$ , we estimate the color excess  $E(B - V)$  from the Balmer decrement, assuming case B, the Cardelli et al. (1989) extinction law, and  $R_V = 4.05$ . We then correct line fluxes

for extinction and compute the line ratios needed to construct standard excitation diagrams (Baldwin et al. 1981; Veilleux & Osterbrock 1987; Kewley et al. 2006). For galaxies without measured nebular extinction, we correct fluxes using the stellar color excess divided by 0.44 (Calzetti et al. 2000). We list the estimated nebular color excess in Table 4, as well as the intrinsic  $[O III]$  and  $H\alpha$  luminosities. Figure 4 shows the excitation diagrams with lines separating emission-line classes; we list the adopted spectral types in Table 4. For the H II galaxy we compute SFR from  $H\alpha$  (Moustakas et al. 2006). For other galaxies, we compute a SFR upper limit, as at least some of the  $H\alpha$  emission arises from processes other than photoionization from young stars.

The excitation diagrams show that the spectral types of ORC1c and ORC4c are most consistent with being low-ionization nuclear emission line regions (LINERs). ORC4c lies in the composite region of the  $[N II]/H\alpha$  versus  $[O III]/H\beta$  diagram (hereafter n2ha), but is squarely in the LINER region of the  $[O I]/H\alpha$  versus  $[O III]/H\beta$  (o1ha) and  $[O I]/H\alpha$  versus  $[O III]/[O II]$  (o3o2) diagrams.  $[O I]$  is more diagnostic of LINER regions because it traces the extended partially-ionized zone of nebulae, and has previously been used to define LINER sub-classes (Sarzi et al. 2010). The low-ionization  $[N I]$  5198, 5200 Å line has also been used to categorize LINERs in nearby ellipticals (Sarzi et al. 2010). In ORC4c,  $[N I]/H\beta = -0.59 \pm 0.17$ , which in combination with  $[O III]/H\beta$  puts it in the same LINER class as other  $z = 0$  massive ellipticals (Sarzi et al. 2010).

ORC23c and ORC5se are unambiguously AGN and star-forming nuclei, respectively. We list ORC5c as an H II/LINER, as its lines are intrinsically weak and the line ratios are uncertain, particularly  $[O III]/H\beta$  and  $[O I]/H\alpha$ . Its placement in the n2ha, s2ha, and o1ha diagrams are consistent with LINER/composite, H II, and H II/LINER within the  $1\sigma$  errors, respectively.

### 3.2. Spectral Energy Distributions

As we did in Coil et al. (2024) for ORC4c, we use the Tractor photometry to perform Prospector (Johnson et al. 2021) fits to the rest-frame optical-to-near-infrared spectral energy distribution of each source with a known redshift. We fit to the observed-frame *griz* and W1/W2 photometry. Prospector infers the properties of the galaxy’s stars through gridless Bayesian parameter estimation and Markov chain Monte Carlo (MCMC) posterior sampling with `emcee` (Foreman-Mackey et al. 2013). The starlight models are generated with Flexible Stellar Population Synthesis (FSPS; Conroy et al. 2009; Conroy & Gunn 2010). The goal of these fits is not to reconstruct an accurate star formation history for each

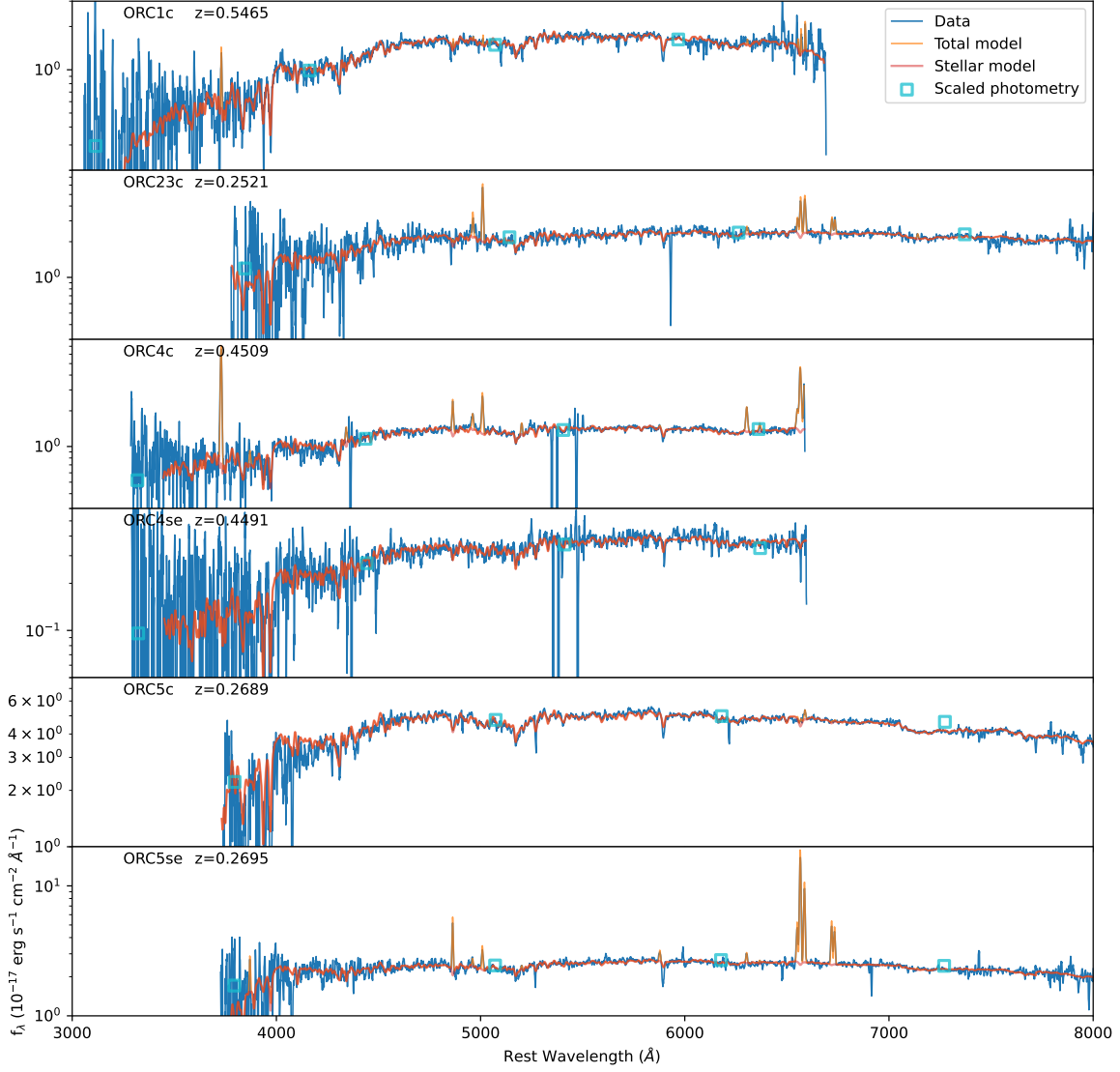


**Figure 2.** Rest-frame spectra of the six galaxies with identifiable redshifts. The data (blue) are smoothed with a 5-pixel boxcar; the continuum model (red) and emission-line model (orange) are overplotted. Photometry (cyan boxes) is shown, scaled down by the mean  $r + i$  slit loss  $f_{p/s}$  (Column 7 of Table 2).

source, but rather to estimate the stellar mass, to get some constraints on current and recent star formation, and to put further constraints on any current AGN activity.

We assume a Kroupa initial mass function (Kroupa 2001) and a power law attenuation  $A_\lambda/A_V \sim \lambda^{-0.7}$  that matches the Milky Way’s UV-to-optical slope (Salim &

Narayanan 2020). To parameterize the star formation history, we use a delayed  $\tau$ -model such that SFR declines as  $t_{\text{age}} e^{-t_{\text{age}}/\tau}$ , where  $t_{\text{age}}$  is the galaxy’s age. We set a log-uniform prior on  $t_{\text{age}}$  such that the galaxy is not younger than 100 Myr when observed and doesn’t form before the Universe ( $0.1 \text{ Gyr} < t_{\text{age}} < t_{\text{Universe}}(z)$ , where  $t_{\text{Universe}}(z)$  is the age of the Universe at the galaxy’s

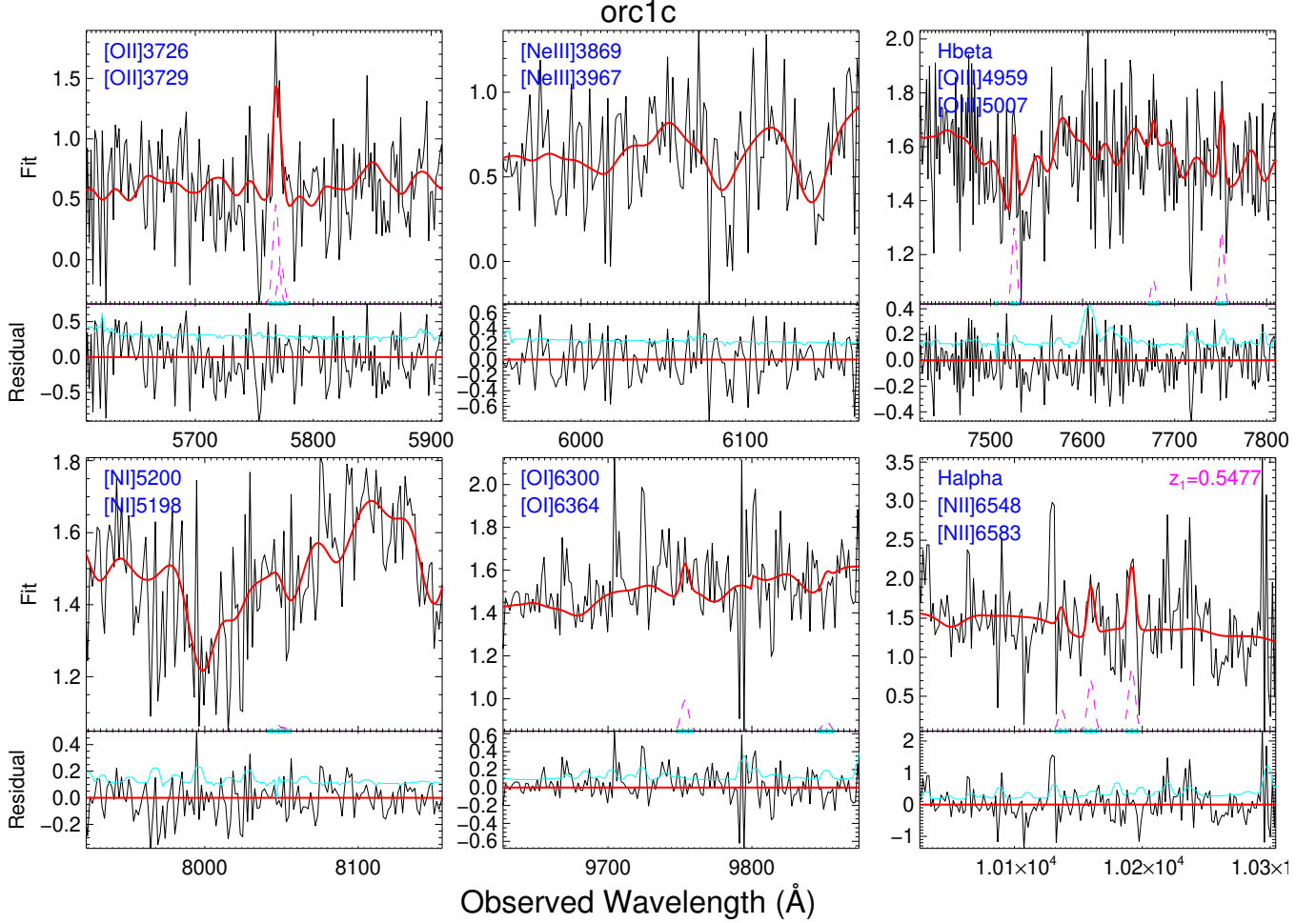


**Figure 3.** Spectra of galaxies with detectable line emission, displayed to highlight individual lines. The upper portion of each panel (“Fit”) shows the data (black); the best-fit model (red); the emission line model (dashed magenta); and the wavelength range masked during continuum fitting (cyan bars). The lower portion (“Residual”) shows the data minus the model, in addition to  $1\sigma$  error spectra (cyan). Lines that may appear in the wavelength range of each panel are listed in the upper left corner of that panel.

redshift  $z$ ). We allow the bolometric fraction of the light due to Type I AGN to be a free parameter. The stellar mass  $M_*$  is a free parameter, with a log-normal prior with a mode of  $\ln(M_*/M_\odot) = 25$  and a dispersion of 15. Finally, we update the stellar metallicity for each random draw of  $M_*$  to be within  $\pm 0.1$  dex of the mass-metallicity relation (Ma et al. 2016).

For ORC 5se, which is clearly a star-forming galaxy rather than an AGN (Section 4.1), we set the AGN fraction to zero and allow a recent burst.

We list the best-fit parameters and  $1\sigma$  errors in Table 5. We also compute and list the current star formation rate and star formation rate 1 Gyr in the past using

$$\begin{aligned} \text{SFR} &= \text{SFR}_{\text{max}} \frac{t_{\text{age}}}{\tau} (e^{1-t_{\text{age}}/\tau}) \\ \text{SFR}_{\text{max}} &= M_* (e^{-1} \times 10^{-9} M_\odot \text{ yr}^{-1}) \times \end{aligned} \quad (1)$$

$$\tau^{-1} [1 - (1 + \frac{t_{\text{age}}}{\tau}) e^{-t_{\text{age}}/\tau}]^{-1} \quad (2)$$

where  $t_{\text{age}}$  and  $\tau$  are in Gyr and  $M_*$  is in  $M_\odot$ .

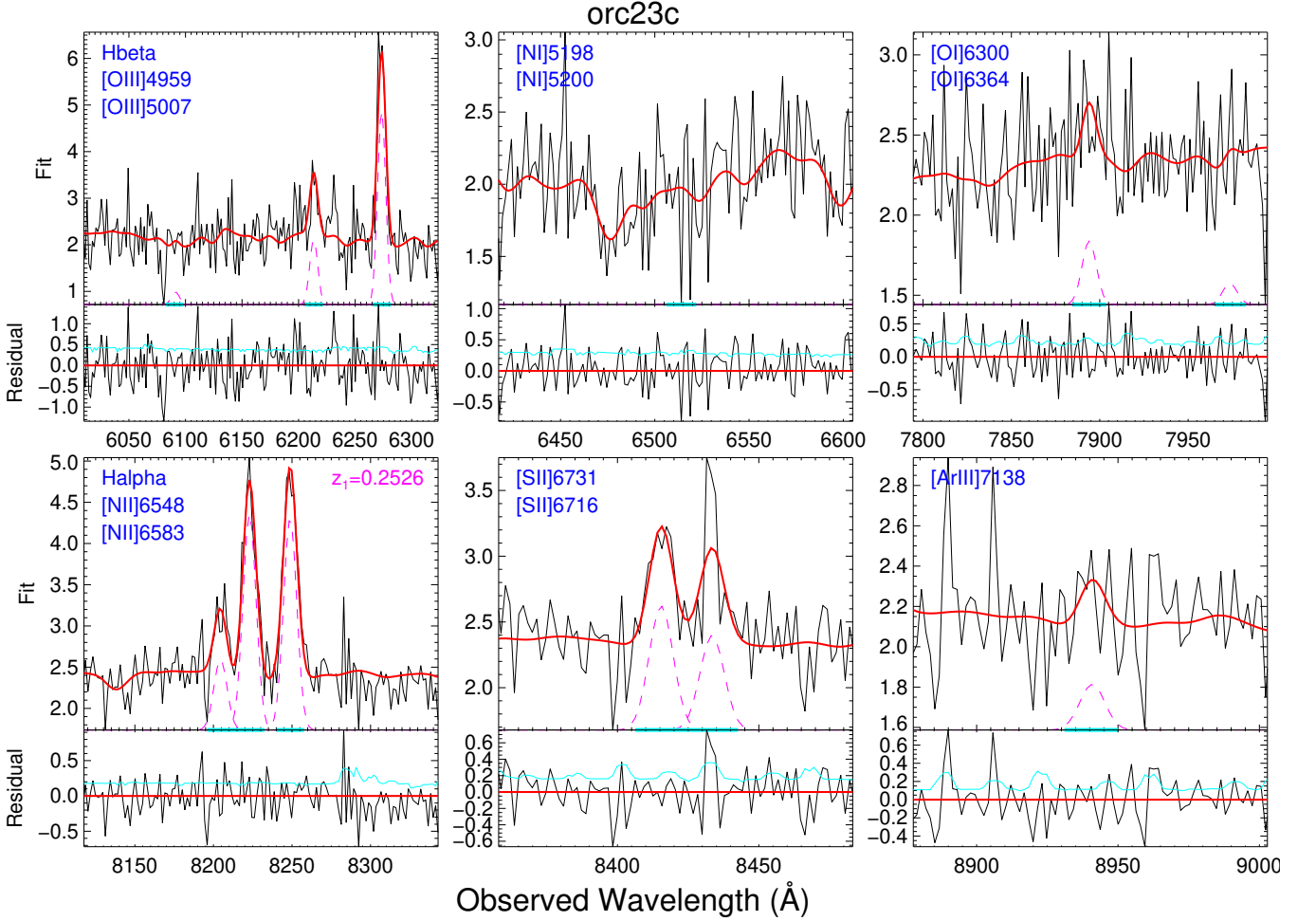
This differs from our methodology in Coil et al. (2024), in which for ORC4c. In that fit, we incorporated additional  $u$ -band data to However, the results are consistent—the inferred masses are the same 1 Gyr in the past—like the elevated SFR we find 1 Gyr in the galaxy

## 4. DISCUSSION

### 4.1. Characterizing the galaxies of ORCs 1–5

We are now in a position to characterize the properties of the central galaxies of ORCs, as well as other, possibly related, galaxies in or near the ORC footprints. This provides stronger constraints on the possible origin of these phenomena, as well as the intrinsic sizes of the circles.




 Figure 3. *Continued.*

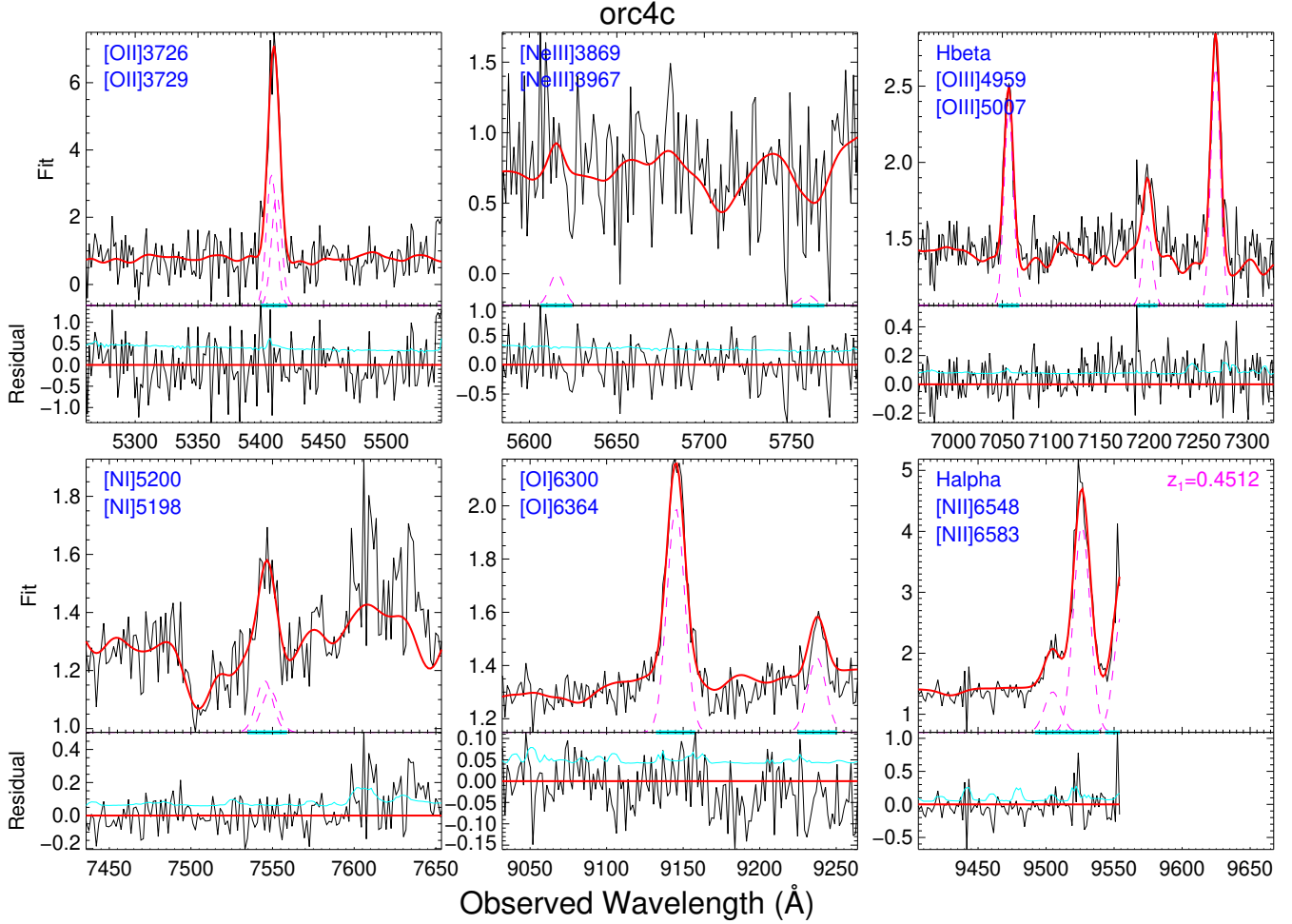
The three isolated ORCs in our study (ORC1, ORC4, and ORC5) each have a central source well outside the local Universe ( $z = 0.547$ ,  $0.451$ , and  $0.270$ ). These measurements confirm or refine initial estimates from photometry (Norris et al. 2021b; Koribalski et al. 2021; Norris et al. 2022). For ORC4c, the initial photometric redshift estimate of  $z = 0.385$  was significantly smaller than the spectroscopic redshift (Coil et al. 2024).

Besides their distances, the systems ORC1c, ORC4c, and ORC5c are remarkably similar in other ways. They are red elliptical galaxies with no internal stellar attenuation (Tables 2 and 4). Following Norris et al. (2022), we verify that their  $g-r$ ,  $r-i$ ,  $W1-W2$ , and  $W2-W3$  colors<sup>4</sup> (Table 3) are consistent with early type galaxies, with no evidence for AGN activity (Jarrett et al. 2019; Yao et al. 2020). Their light-weighted stellar populations are dominated by stars with ages  $> 1$  Gyr (80-

100% of the light at rest-frame 5000 Å; Table 4). They have velocity dispersions  $225 - 250 \text{ km s}^{-1}$  (Table 4), roughly consistent with the stellar masses from SED fitting of  $M_* = 2 - 5 \times 10^{11} M_\odot$  (Table 5). They each have some nebular emission, and spectral types consistent with LINER (Table 4). Based on the Prospector fits, there is no evidence for a luminous AGN in the optical and near-infrared (Table 5).

ORC1c and ORC5c have  $H\alpha$  luminosities ( $\log[L_{H\alpha}/L_\odot] = 40.5 - 40.6$ ; Table 4) that are about  $10\times$  higher than  $z = 0$  ellipticals of comparable mass (Sarzi et al. 2006; Cappellari et al. 2006). The excess could arise due to shocks, as we discuss below. However, even if they were powered by stellar photoionization, the implied SFR is negligible (Table 4). The WISE W3 non-detections give  $1\sigma$  upper limits of  $15$  and  $4 M_\odot \text{ yr}^{-1}$ , respectively (Cluver et al. 2017), that are less stringent. Their SEDs are consistent with little star formation over the last Gyr (Table 5), as are their Balmer break  $D_n(4000)$  indices (Table 4; Kauffmann et al. 2003a).

<sup>4</sup> We compute WISE colors in the Vega system for literature comparison using Cutri et al. (2012).

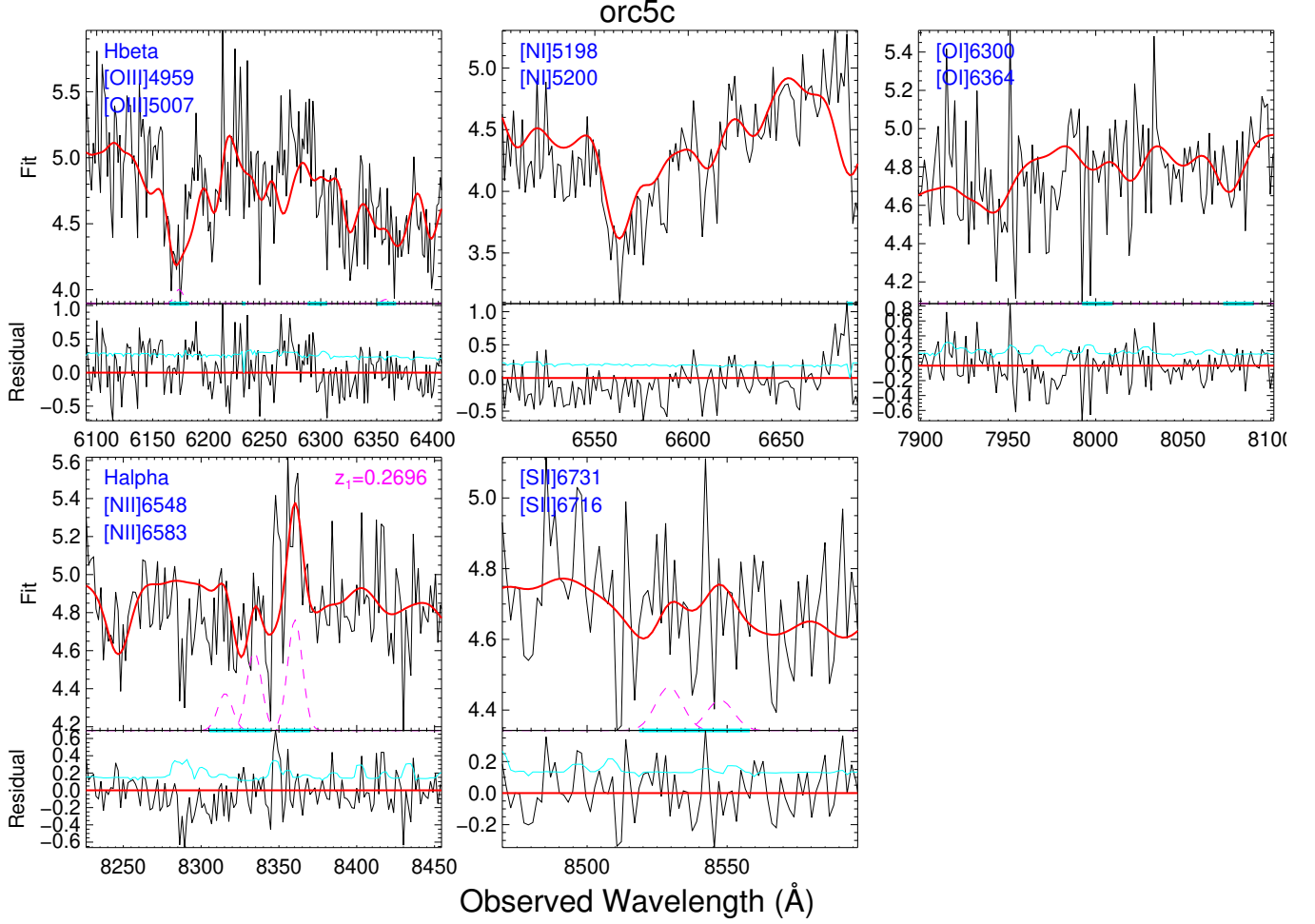
Figure 3. *Continued.*

ORC4c is unique among these three central galaxies in that its H $\alpha$  emission is about  $10\times$  brighter than that of ORC1c and ORC5c (Table 4). In the [O II] 3727, 3729 Å line, it is particularly luminous ( $W_{\text{eq}} = 50$  Å), extended over 40 kpc, and turbulent ( $\sigma_{\text{gas}} = 180$  km s $^{-1}$ ; Coil et al. 2024). With our longslit data, we recover about 80% of the flux observed with KCWI and a similar velocity dispersion (Table 4; Coil et al. 2024). In comparison, the emission lines in ORC1c are unresolved, while those in ORC5c have  $\sigma_{\text{gas}} = 142 \pm 31$  km s $^{-1}$  (Table 4). The star formation rate in ORC4c is low, with  $\text{SFR} < 5 - 7$  M $_{\odot}$  yr $^{-1}$  from H $\alpha$  (Table 4) and WISE W3 (Cluver et al. 2017). However, the SFR may have been significantly elevated sometime in the last Gyr. The spectrum indicates some contribution from young stars (Table 4), and the parameterized star-formation history from SED modeling shows a decrease in the SFR from 30 to 1 M $_{\odot}$  yr $^{-1}$  over the past Gyr (Table 5). Using additional  $u$ -band data, the more detailed star-formation history of ORC1c presented in Coil et al. (2024) is consistent with an intense starburst about 1 Gyr ago, as

is its lower  $D_n(4000)$  value (Table 4; Kauffmann et al. 2003a).

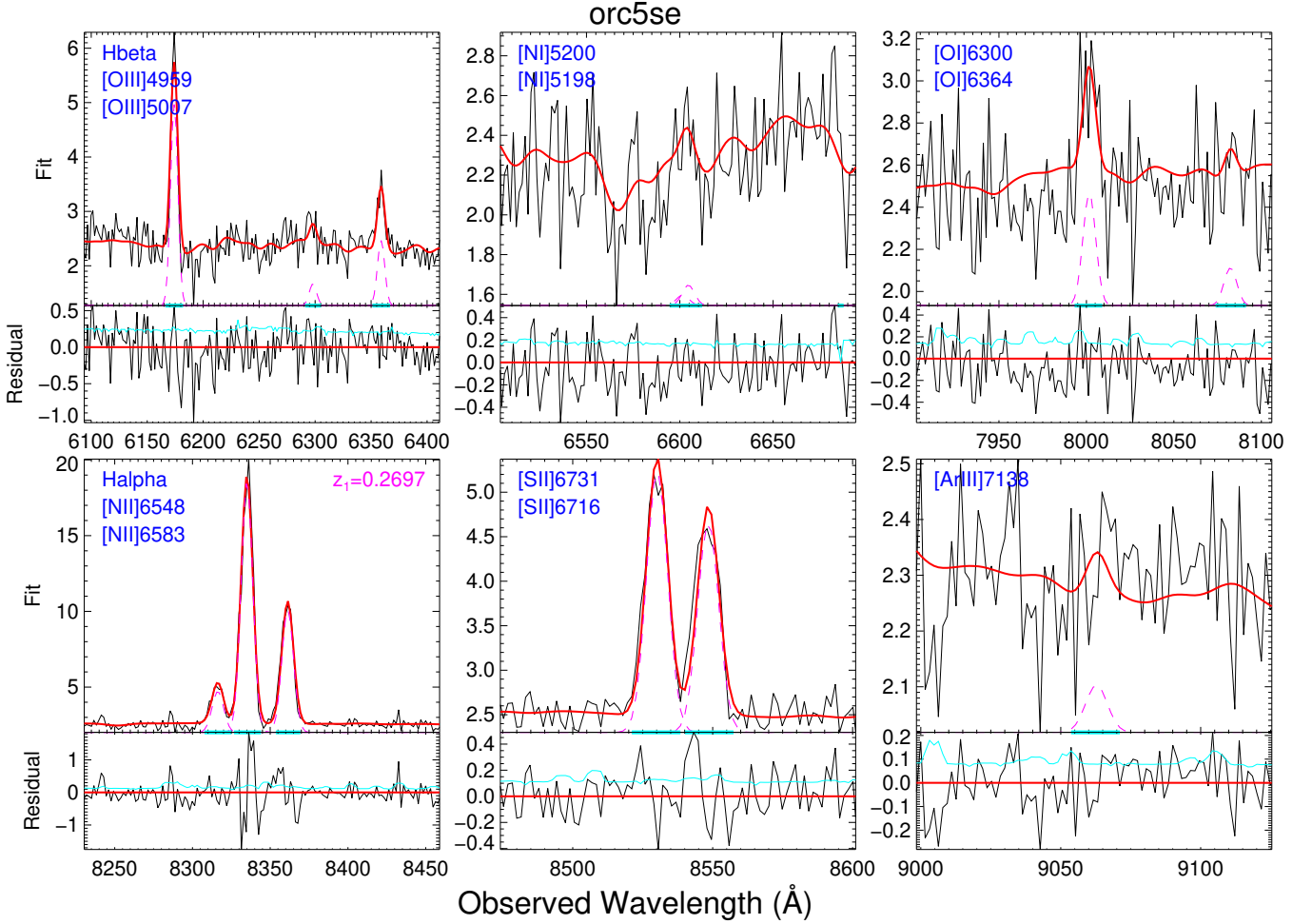
The radio emission in these galaxies is in excess of that expected from star formation. Coil et al. (2021) argue for radio AGN in ORC1c, ORC4c, and ORC5c based on the radio excess (radio flux density at 1.4 GHz divided by the star formation rate estimated from the radio and other tracers). Our star formation rate is lower than those of Norris et al. (2022), and thus strengthen this conclusion. The radio emission is brighter than expected from star formation in these sources by 1–2 orders of magnitude. Even with the upper limits, the lower limits on the 1.4 GHz excess ( $L_{1.4}/L_{1.4, \text{SFR}}$ ) are high for ORC1c, ORC4c, and ORC5c. Radio sources like ORC1c, ORC4c, and ORC5c that do not have an excess of hot dust (based on WISE colors), but that do have a significant number of true AGNs (Yao et al. 2022).

LINER-like emission can arise from multiple physical processes. We argue below that the emission in ORC4c, and perhaps also 1c and 5c, is shock-dominated (Section 4.2). However, the LINER classifications of ORCs 1c, 4c, and 5c are also consistent with an AGN in these sources. We combine our optical data with the radio results using the AGN classification scheme of Best &


 Figure 3. *Continued.*

Heckman (2012). In Figure 5, we show where these galaxies fall in two parts of this scheme; the third is based on the n2ha diagram (Figure 4). The scheme places these galaxies in the radio-quiet AGN class. (Formally, ORC 5c is in the radio-loud AGN class, but its  $D_n(4000)$  has a large error bar that overlaps the radio-quiet class; its low radio luminosity is more consistent with the radio-quiet class.) Following Best & Heckman (2012), we compute the Eddington ratio in these sources by combining the AGN power in radiation and mechanical jet power. We apply a bolometric correction of 142 to  $L_{[\text{OIII}]}$  (Lamastra et al. 2009) and use the calibration of Heckman & Best (2014) to compute the radio jet power. The result is a low Eddington ratio:  $\log(L/L_{\text{Edd}}) = -3$  to  $-4$ . These values are consistent with radiatively-inefficient accretion, as observed in lower-luminosity AGN (Ho 2009). The Eddington ratio of these systems is even lower if the line (and/or radio) emission is dominated by shocks, an effect which is likely strongest in ORC 4c. Our spectra uncover two other galaxies within the radio footprints of ORCs 4

and 5 that lie at the same redshift as the central source. ORC4se is another old, red elliptical (Tables 2, 4, and 5) with no nebular emission or star formation detected (Table 4). It lies at a projected distance of 35 kpc from ORC4c (Table 2), and is about  $6\times$  less massive ( $\sigma_* = 166 \pm 18 \text{ km s}^{-1}$ ,  $\log[M_*/M_\odot] = 10.6$ ; Tables 4 and 5). ORC5se lies at the edge of ORC5 radio ring, at a projected distance of 151 kpc from ORC5c (Table 2). It is a spheroidal system (Table 2) classified as a star-forming galaxy (Figure 4). Its spectrum has a significant contribution from a young, modestly obscured stellar population (Table 4). Like ORC5c, it is massive ( $\sigma_* = 263 \pm 33 \text{ km s}^{-1}$  and  $\log[M_*/M_\odot] = 11.0$ ; Tables 4 and 5). Its star formation rate is  $57 M_\odot \text{ yr}^{-1}$  based on  $\text{H}\alpha$  (Table 4),  $22 \pm 16 M_\odot \text{ yr}^{-1}$  based on W3 (Cluver et al. 2017), and  $27 \pm 3$  from radio emission (Table 6). The SED fit points to a burst in the last 2 Gyr (Table 5), consistent with the  $D_n(4000)$  value (Table 4; Kauffmann et al. 2003a), but is not sensitive to the ongoing star formation.

Figure 3. *Continued.*

ORCs 2 and 3 have no central galaxies. We observed the system directly between them, which is a disk galaxy at  $z = 0.252$  (Table 4), somewhat closer than the previous photometric estimate ( $z = 0.286$ ; Norris et al. 2021b). We discuss below whether ORC23c is related to ORCs 2 and 3. However, if we do associate ORC23c with ORCs 2 and 3 and assume they all lie at the same redshift, then ORC23c is 168 kpc in projection from the center of ORC2 and 274 kpc from the center of ORC3 (Table 2 and Norris et al. 2021b). This system also hosts an old stellar population (Table 4), but in this case with a Type 2 AGN (Figure 4). Its bolometric luminosity (based on  $L_{[\text{OIII}]}$ ; Table 4) and Eddington ratio (Table 6) are the highest in the sample. It is firmly in the radio-quiet AGN category (Figure 5; (Best & Heckman 2012)) along with ORC1c, 4c, and 5c, but with a higher radiative vs. jet output.

#### 4.2. Origins of the ORC phenomenon

The confirmed redshifts of the central galaxies of ORCs 1, 4, and 5 rule out a Galactic origin. The in-

trinsic diameters of the ORCs inferred from these redshifts are thus in the range 300-500 kpc, as previously inferred based on photometric redshifts (Norris et al. 2022). They instead point to one of the various mechanisms that have been proposed that involve galaxy-wide processes. These include a powerful wind shock propagating into the CGM (Norris et al. 2022; Coil et al. 2024), shocks driven by the gravitational motions in a galaxy merger (Dolag et al. 2023), or a virial shock (Yamasaki et al. 2024).

In Coil et al. (2024), we argue for a galactic wind model for ORC4c based on the morphology, kinematics, and luminosity of the extended line emission. We also show that a 2D hydrodynamic model of a blast wave driven for 200 Myr by a  $200 M_{\odot} \text{ yr}^{-1}$  starburst, or alternatively a luminous AGN, can reproduce the optical and radio data. In this scenario, the large-scale radio emission is produced by the forward shock and observed 800 Myr after the wind begin. The ionized gas was reheated by the reverse wind shock and by further shocks as it fell back on to the central galaxy.



**Table 4.** Galaxy Properties Derived from Spectra

Label	$z_*$	$z_{\text{gas}}$	$\sigma_*$	$\sigma_{\text{gas}}$	Spec. Type	$\log L_{[\text{OIII}]}$
			km s <sup>-1</sup>	km s <sup>-1</sup>		erg s <sup>-1</sup>
(1)	(2)	(3)	(4)	(5)	(6)	(7)
ORC1c	$0.54652 \pm 0.00005$	$0.54766 \pm 0.00010$	$249 \pm 13$	...	LINER	$40.28^{+0.14}_{-0.21}$
ORC23c	$0.25213 \pm 0.00008$	$0.25262 \pm 0.00002$	$196 \pm 22$	$121 \pm 6$	AGN	$41.91^{+0.04}_{-0.05}$
ORC4c	$0.45089 \pm 0.00004$	$0.45115 \pm 0.00002$	$227 \pm 11$	$172 \pm 2$	LINER	$41.44^{+0.04}_{-0.04}$
ORC4se	$0.44914 \pm 0.00006$	...	$166 \pm 20$	...	...	...
ORC5c	$0.26887 \pm 0.00004$	$0.26956 \pm 0.00013$	$233 \pm 11$	$142 \pm 31$	HII/LINER	$< 39.40^{+0.72}$
ORC5se	$0.26961 \pm 0.00008$	$0.26969 \pm 0.00000$	$263 \pm 33$	$100 \pm 1$	HII	$41.85^{+0.06}_{-0.07}$

$\log L_{\text{H}\alpha}$	SFR	$E(B - V)_*$	$E(B - V)_{\text{gas}}$	$D_n(4000)$	young	int.	old	$\log M_{\text{BH}}$
erg s <sup>-1</sup>	M <sub>⊙</sub> yr <sup>-1</sup>	mag	mag		%	%	%	M <sub>⊙</sub>
(8)	(9)	(10)	(11)	(12)	(13)	(14)	(15)	(16)
$40.54^{+0.17}_{-0.29}$	$< 0.3^{+0.2}$	$0.02 \pm 0.01$	...	$1.66 \pm 0.04$	0	14	82	$8.86 \pm 0.33$
$41.68^{+0.03}_{-0.04}$	$< 3.7^{+0.0}$	$0.11 \pm 0.02$	...	$1.04 \pm 0.47$	0	0	99	$8.28 \pm 0.41$
$41.81^{+0.03}_{-0.03}$	$< 5.1^{+0.0}$	$0.00 \pm 0.01$	$0.15 \pm 0.05$	$1.30 \pm 0.05$	7	0	79	$8.64 \pm 0.33$
...	...	$0.11 \pm 0.04$	...	$2.34 \pm 0.03$	0	0	100	$7.88 \pm 0.42$
$40.59^{+0.10}_{-0.13}$	$< 0.3^{+0.1}$	$0.00 \pm 0.01$	...	$2.29 \pm 0.29$	0	0	100	$8.70 \pm 0.32$
$42.85^{+0.03}_{-0.03}$	$56.5 \pm 3.7$	$0.19 \pm 0.02$	$0.55 \pm 0.05$	$1.44 \pm 0.25$	43	0	57	$9.00 \pm 0.43$

NOTE—Column 1: Label from Figure 1. Columns 2–5: Stellar and ionized gas redshifts and velocity dispersions. Errors shown are  $1\sigma$ . Redshifts are heliocentric and velocity dispersions intrinsic (corrected for instrumental effects). Column 6: Adopted spectral type. Columns 7–8: Extinction-corrected [O III] 5007 Å and H $\alpha$  luminosities. Where nebular extinction is not available, we correct using  $E(B - V)_{\text{gas}} = E(B - V)_*/0.44$  (Calzetti et al. 2000). Column 9: Star formation rate from H $\alpha$  (Moustakas et al. 2006). Set to upper limit if not an HII spectral type. Column 10: Stellar broadband colour excess derived from ppxf fits that use the Calzetti et al. (2000) attenuation curve with  $R_V = 4.05$ . We estimate the  $1\sigma$  error with Monte Carlo simulations. Column 11: Nebular broadband colour excess and  $1\sigma$  error, derived from H $\alpha$ /H $\beta$  decrement assuming Case B conditions, the Cardelli et al. (1989) extinction curve, and  $R_V = 4.05$ . Column 12: The Balmer break index as defined in Balogh et al. (1999). Columns 13–15: Percentage contribution to the total starlight model at rest-frame 5000 Å in bins of young (<100 Myr), intermediate-age (100 Myr – 1 Gyr), and old (>1 Gyr) populations. The sum may be less than 100% if there is an additive polynomial contribution. Column 16: Black hole mass estimated from  $\sigma_*$  (McConnell & Ma 2013). Error includes measurement error in  $\sigma_*$  and the scatter in the  $M_{\text{BH}} - \sigma$  relation.

It is likely that in ORC4c, the line emission—and possibly also the central radio emission—have a dominant contribution from extended shocks. Its line ratios and line widths are consistent with those seen, for instance, in the extended regions of the giant relic wind around the starburst galaxy Makani (Rupke et al. 2023). The rest-frame equivalent width of the [O II] 3727, 3729 Å emission in this source is 50 Å Coil et al. (2024), which is  $10\times$  higher than in other massive ellipticals (Pandya et al. 2017). If shocks dominate  $L_{1.4}$  and/or  $L_{[\text{OIII}]}$ , the estimated Eddington ratio is an upper limit (Table 6).

Though they overlap with ORC4c in excitation diagrams (Figure 4), the origin of the LINER emission in ORC1c and 5c is murkier due to their lower line luminosities and widths. One possibility is shocks in a relic wind, as we hypothesize for ORC4c. Others include photoionization and shock emission from a low-luminosity AGN (e.g., Molina et al. 2018) or photoionization by evolved stars (e.g., Sarzi et al. 2010). The H $\alpha$  luminosities of ORC1c and ORC5c are  $\sim 10\times$  smaller than that of ORC4c (Table 4), though still  $10\times$  higher than comparably massive,  $z = 0$  ellipticals (Sarzi et al. 2006). Their

line equivalent widths are also lower than in ORC4c; we measure  $W_{\text{eq}}^{\text{rest}} = 9 \text{ Å}$  for [O II] in ORC1c, which is consistent with other massive galaxies (Pandya et al. 2017). The central radio luminosity of ORC4c is higher than in ORC1c and ORC5c by factors of a few to  $\sim 10$  (Table 6), which could point to a larger shock contribution. Finally, the [O III] equivalent widths of ORC1c and ORC4c differ by a factor of 5–10, consistent with a higher contribution of shocks to  $L_{[\text{OIII}]}$ , as well, in ORC4c compared to ORC1c.

Despite these differences in line luminosity, the other similarities of the central galaxies of the three ORCs may point to a common origin. If it is in a starburst or AGN blast wave, then the current radio emission must have moved at modest speeds to the currently observed radii of 150–250 kpc. If it is due to a starburst, the burst appears to be in the distant past ( $\gtrsim 1$  Gyr ago). The ballistic flow speed over 1 Gyr is 150–250 km s<sup>-1</sup> for 150–250 kpc. This is remarkably similar to the inferred flow speeds for the clearly wind-powered nebula in Makani (Rupke et al. 2019). If the radio bubbles were instead powered by an AGN event, any evidence would have dis-

**Table 5.** Galaxy Properties Derived from SED Fits

Label	$\log(M_*/M_\odot)$	$t_{\text{age}}$	$\tau$	SFR <sub>now</sub>	SFR <sub>1 Gyr</sub>	AGN fraction
		Gyr	Gyr	$M_\odot \text{ yr}^{-1}$	$M_\odot \text{ yr}^{-1}$	
(1)	(2)	(3)	(4)	(5)	(6)	(7)
ORC1c	$11.7 \pm 0.3$	$1.52^{+0.05}_{-0.03}$	$0.02^{+0.02}_{-0.01}$	0.0	0.0	$0.01^{+0.01}_{-0.01}$
ORC23c	$11.2 \pm 0.3$	$10.3^{+0.2}_{-0.4}$	$1.40^{+0.03}_{-0.06}$	0.5	1.0	$0.18^{+0.03}_{-0.03}$
ORC4c	$11.4 \pm 0.3$	$2.3^{+0.2}_{-0.2}$	$0.26^{+0.04}_{-0.04}$	1.2	33	$0.00^{+0.01}_{-0.00}$
ORC4se	$10.6 \pm 0.3$	$3.4^{+0.8}_{-0.5}$	$0.23^{+0.17}_{-0.15}$	0.0	0.0	$0.06^{+0.10}_{-0.05}$
ORC5c	$11.2 \pm 0.3$	$2.98^{+0.06}_{-0.07}$	$0.19^{+0.02}_{-0.02}$	0.0	0.3	$0.00^{+0.00}_{-0.00}$
ORC5se	$11.0 \pm 0.3$	$10.17^{+0.11}_{-0.27}$	$1.98^{+0.06}_{-0.07}$	... <sup>a</sup>	... <sup>a</sup>	$0.0^a$

NOTE—Column 1: Label. Column 2: Best-fit stellar mass from Prospector fits; we assign a conservative factor-of-two error. Columns 3–4: Best-fit parameters for a delayed- $\tau$  star formation history  $t_{\text{age}} e^{-t_{\text{age}}/\tau}$ . Columns 5–6: Current SFR and SFR 1 Gyr in the past from best-fit star formation history. Column 7: Best-fit AGN fraction.

<sup>a</sup>For this galaxy we do not include an AGN and instead add a burst to the model. The best-fit burst parameters are for  $33^{+0.03}_{-0.05}\%$  of the galaxy mass to have formed at  $0.84 \pm 0.01$  of the galaxy’s current age, which is roughly 1.6 Gyr in the past.

**Table 6.** Radio Properties

Label	$\nu_{\text{obs}}$	$S_{\nu, \text{obs}}$	$\alpha$	$\nu_{1.4}$	$S_{\nu, 1.4}$	$L_{1.4}$	$L_{1.4}/L_{1.4, \text{SFR}}$	$\log(L/L_{\text{Edd}})$
	GHz	mJy		GHz	mJy	$10^{22} \text{ W Hz}^{-1}$		
(1)	(2)	(3)	(4)	(5)	(6)	(7)	(8)	(9)
ORC1c	1.284	$0.091 \pm 0.004$	$-1.40 \pm 0.05$	0.905	$0.15 \pm 0.01$	$12.2 \pm 0.7$	$> 292 \pm 142$	$-3.74 \pm 0.37$
ORC23c	0.944	$0.19 \pm 0.05$	$-1.23 \pm 0.36$	1.118	$0.15 \pm 0.04$	$2.6 \pm 0.7$	$> 4 \pm 1$	$-2.30 \pm 0.46$
ORC4c	0.325	$1.43 \pm 0.13$	$-0.92 \pm 0.18$	0.965	$0.53 \pm 0.21$	$29 \pm 12$	$> 37 \pm 15$	$-2.93 \pm 0.34^a$
ORC5c	0.944	$0.10 \pm 0.03$	$-0.8 \pm 0.2$	1.103	$0.09 \pm 0.03$	$1.7 \pm 0.5$	$> 35 \pm 14$	$< -4.20^{+0.78}$
ORC5se	0.944	$0.25 \pm 0.03$	$-0.8 \pm 0.2$	1.103	$0.22 \pm 0.03$	$4.2 \pm 0.6$	$0.49 \pm 0.07$	...

NOTE—Column 1: Label. Column 2–4: Observed frequency, flux density, and spectral index (Norris et al. 2021b; Koribalski et al. 2021; Norris et al. 2022), where  $S_\nu \sim \nu^\alpha$ . Where not explicitly listed in the literature, flux errors are assumed to be twice the r.m.s. sensitivity per beam. Column 5–6: Observed frequency corresponding to 1.4 GHz in the galaxy’s rest frame and flux density at this frequency extrapolated from  $S_{\nu, 1.4} = S_{\nu, \text{obs}}(\nu_{\text{obs}}/\nu_{1.4})^\alpha$ . Column 7: Luminosity density at 1.4 GHz in the galaxy’s rest frame, in units of  $10^{22} \text{ W Hz}^{-1}$ :  $L_{1.4} = 4\pi d_L^2 S_{\nu, 1.4}/(1+z)$ , where  $d_L$  is the luminosity distance. Column 8: Excess 1.4 GHz emission above that expected from star formation. The SFR is from H $\alpha$  (Table 4), which provides only upper limits for most sources. We convert SFR to  $L_{1.4, \text{SFR}}$  using the calibration from Matthews et al. (2021), assuming a Salpeter IMF to match the H $\alpha$  SFR calibration of Moustakas et al. (2006). The errors are propagated from the fluxes and do not include systematics in the calibration. Column 9: Eddington ratio, where the observed luminosity combines radiation and jet power. We use an [O III] 5007 Å bolometric correction of 142 (Lamastra et al. 2009) for radiation and equation (2) of Heckman & Best (2014) for the radio jet power.

<sup>a</sup>This is an upper limit if shocks contribute significantly to  $L_{[\text{OIII}]}$  and/or  $L_{1.4}$ .

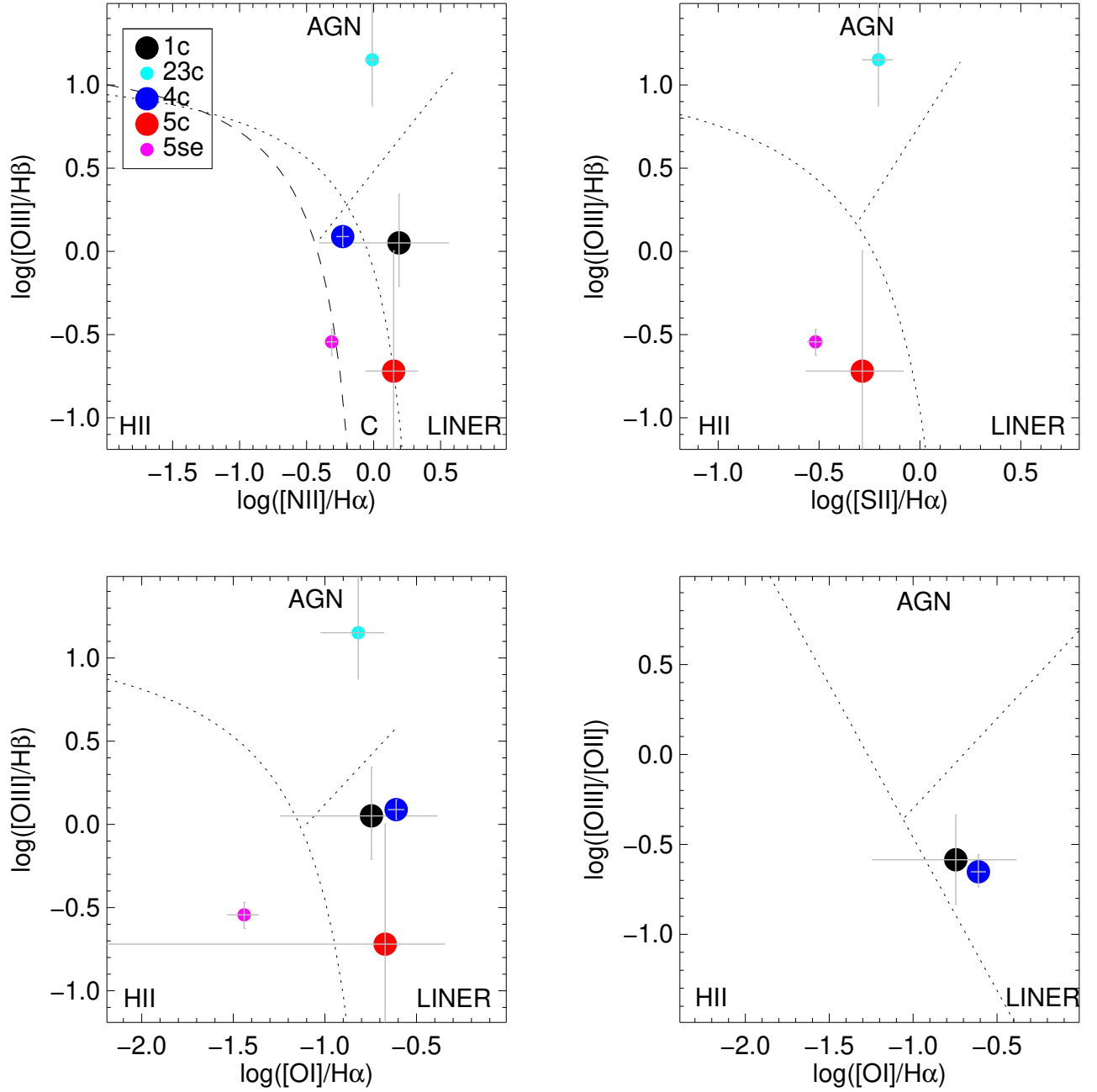


**Figure 4.** Standard excitation diagrams (Baldwin et al. 1981; Veilleux & Osterbrock 1987; Kewley et al. 2006) for the five identified galaxies with emission lines. The dashed and dotted lines divide nuclear classification regions of star-forming (H II), AGN, Low-Ionization Nuclear Emission Line Region (LINER), and composite (C) using canonical dividing lines (Kauffmann et al. 2003b; Kewley et al. 2006; Cid Fernandes et al. 2010). The adopted spectral type of each source is listed in Table 4.

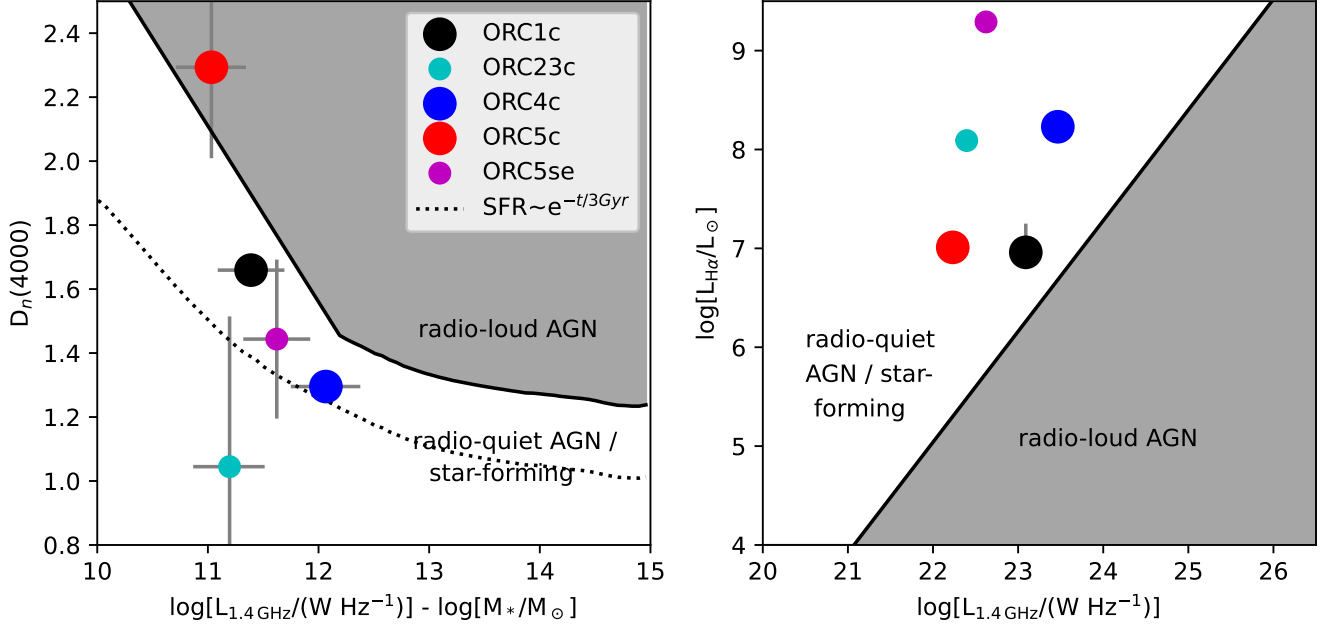


**Figure 5.** Two parts of the radio-based galaxy classification scheme of Best & Heckman (2012); the third uses the n2ha excitation diagram (Figure 4). The dashed line is the evolutionary track of a galaxy with an exponentially-declining star formation rate with e-folding time 3 Gyr (Bruzual & Charlot 2003). The solid lines divide radio-loud AGN from radio-quiet AGN and star-forming galaxies. We digitized the dividing line in the  $D_n(4000)$  vs.  $L_{1.4} - M_*$  diagram from Best & Heckman (2012) using WebPlotDigitizer (Rohatgi 2022).

appeared more quickly, and the constraints on timescale are weaker. That said, an energetic AGN event would probably also coincide with significant star formation (Schweitzer et al. 2006; Aird et al. 2019), which we conclude is well in the past. In the blastwave scenario, we speculate that in ORC1c and ORC5c, the lower luminosity of the ionized gas results from reduced shock emission due to an event occurring further in the past.

Aside from the blastwave scenario, the current data do not provide further constraints on other extragalactic models, such as the galaxy merger (Dolag et al. 2023) or virial shock (Yamasaki et al. 2024) models. However, the morphologies, stellar masses, stellar populations, and ionized gas properties point to massive, red elliptical central galaxies in ORCs 1, 4, and 5. These models feature such galaxies, either as a merger remnant or host of a massive halo.

The absence of a central galaxy points to a different origin for ORCs 2/3, as previously argued (Norris et al. 2021b). A scenario where ORCs 2/3 are the lobes of a radio galaxy (ORC23c) would be difficult to support if ORC23c were star-forming (Norris et al. 2021b). However, we find that ORC23c is actually a Type 2 AGN in a massive, red disk. We suggest that the double radio lobe scenario is therefore still possible in this case. If so,

then the projected end-to-end scale of this radio galaxy is 550 kpc.

Other difficulties with this scenario remain, in that the circularity of such lobes is not common, though such systems do exist (Mullin et al. 2008). For instance, as pointed out by Norris et al. (2021b), the lobes of Fornax A are also circular. The resemblance of Fornax A to ORCs 2/3 increases at lower resolution (Ekers et al. 1983), though the end-to-end scale of Fornax A’s lobes is smaller at 200 kpc (using a distance of 20.0 Mpc from surface brightness fluctuations; Blakeslee et al. 2009).

## 5. CONCLUSION

The Odd Radio Circles are an intriguing phenomena discovered in large-area radio surveys. Among origin theories, the possibility that they are relic remnants of energetic events, potentially representing the largest observed galactic winds, is compelling. Here we present optical spectroscopy of all five initial ORC discoveries, covering the three ORCs with central galaxies (1c, 4c, and 5c) and a galaxy located directly between ORCs 2 and 3 (ORC23c). We also observe two galaxies within the ORC 4 and 5 footprints (ORC4se and ORC5se), both of which lie at the same redshift as their central galaxies at projected distances of 35 and 151 kpc, respectively. We combine the spectroscopy with Tractor



modeling from the Legacy Surveys and Prospector fits to the *griz*+W1/W2 photometry.

The distances of the three central host galaxies rule out a Galactic origin, and are consistent with the enormous intrinsic ORC diameters (300–500 kpc) based on photometry (Norris et al. 2022). Combining the optical and radio data, we find that the central hosts are massive, red ellipticals with little or no ongoing star formation. They host low-luminosity, radio-quiet AGN with low Eddington ratios. They are optical LINERs whose line emission is likely powered by shocks in ORC 4c, and which may be shock- or AGN-powered in ORCs 1c and 5c.

Previously, we argued based on optical IFS that the radio and ionized gas properties of ORC4c are consistent with a blast wave arising from a massive star-forming event in the past Gyr (Coil et al. 2024). The current data support this view. The similarities of ORC1c, 4c, and 5c also support a common origin for ORCs 1, 4, and 5. The ionized gas properties of ORC1c and 5c are closer to those of massive ellipticals than those of ORC4c. ORCs 1c and 5c have  $H\alpha$  luminosities about  $10\times$  lower than in ORC4c (but still  $10\times$  higher than comparably massive ellipticals in the local Universe). Unlike ORC4c, in these two galaxies there is no evidence of a starburst event in the last Gyr. Thus, if they share a common origin with ORC 4, ORCs 1 and 5 may be due to an older event in which the resulting ionized gas shock emission has subsided, and in which the propagation speed of the forward shock was slower than in ORC4.

ORCs 2 and 3 likely have a different origin than the ORCs with prominent central galaxies. We find that the galaxy between the two ORCs, ORC23c, is a Type 2 AGN in a massive, red, disk galaxy. This supports the possibility that this double ORC is in fact a double-lobed radio galaxy.

Better constraints on the ionized gas properties of these systems, including possible extended emission requires sensitive and wide-field integral-field spectroscopy. KCWI observations of ORC 4 revealed extended, high-dispersion [O II] emission that advance the blastwave model (Coil et al. 2024). Deeper, spatially-resolved spectra would help distinguish between shock and AGN excitation in ORCs 1 and 4. They could also constrain the nature of ORCs 2 and 3 by probing other, potentially related, galaxies in the field and searching for extended line emission.

The authors thank the Spring 2022 Observational Astronomy class at Rhodes College for workshoping the proposal that led to these observations.

Based on observations obtained at the international Gemini Observatory under Program IDs GN-2022A-FT-108 and GS-2022A-FT-110. Gemini is a program of NSF’s NOIRLab, which is managed by the Association of Universities for Research in Astronomy (AURA) under a cooperative agreement with the National Science Foundation on behalf of the Gemini Observatory partnership: the National Science Foundation (United States), National Research Council (Canada), Agencia Nacional de Investigación y Desarrollo (Chile), Ministerio de Ciencia, Tecnología e Innovación (Argentina), Ministério da Ciência, Tecnologia, Inovações e Comunicações (Brazil), and Korea Astronomy and Space Science Institute (Republic of Korea). The data was downloaded from the Gemini Observatory Archive at NSF’s NOIRLab.

This work was enabled by observations made from the Gemini North telescope, located within the Maunakea Science Reserve and adjacent to the summit of Maunakea. We are grateful for the privilege of observing the Universe from a place that is unique in both its astronomical quality and its cultural significance.

The Legacy Surveys consist of three individual and complementary projects: the Dark Energy Camera Legacy Survey (DECaLS; Proposal ID #2014B-0404; PIs: David Schlegel and Arjun Dey), the Beijing-Arizona Sky Survey (BASS; NOAO Prop. ID #2015A-0801; PIs: Zhou Xu and Xiaohui Fan), and the Mayall z-band Legacy Survey (MzLS; Prop. ID #2016A-0453; PI: Arjun Dey). DECaLS, BASS and MzLS together include data obtained, respectively, at the Blanco telescope, Cerro Tololo Inter-American Observatory, NSF’s NOIRLab; the Bok telescope, Steward Observatory, University of Arizona; and the Mayall telescope, Kitt Peak National Observatory, NOIRLab. Pipeline processing and analyses of the data were supported by NOIRLab and the Lawrence Berkeley National Laboratory (LBNL). The Legacy Surveys project is honored to be permitted to conduct astronomical research on Iolkam Du’ag (Kitt Peak), a mountain with particular significance to the Tohono O’odham Nation.

LBNL is managed by the Regents of the University of California under contract to the U.S. Department of Energy.

This project used data obtained with the Dark Energy Camera (DECam), which was constructed by the Dark Energy Survey (DES) collaboration. Funding for the DES Projects has been provided by the U.S. Department of Energy, the U.S. National Science Founda-

## ACKNOWLEDGMENTS

tion, the Ministry of Science and Education of Spain, the Science and Technology Facilities Council of the United Kingdom, the Higher Education Funding Council for England, the National Center for Supercomputing Applications at the University of Illinois at Urbana-Champaign, the Kavli Institute of Cosmological Physics at the University of Chicago, Center for Cosmology and Astro-Particle Physics at the Ohio State University, the Mitchell Institute for Fundamental Physics and Astronomy at Texas A&M University, Financiadora de Estudos e Projetos, Fundacao Carlos Chagas Filho de Amparo, Financiadora de Estudos e Projetos, Fundacao Carlos Chagas Filho de Amparo a Pesquisa do Estado do Rio de Janeiro, Conselho Nacional de Desenvolvimento Cientifico e Tecnologico and the Ministerio da Ciencia, Tecnologia e Inovacao, the Deutsche Forschungsgemeinschaft and the Collaborating Institutions in the Dark Energy Survey. The Collaborating Institutions are Argonne National Laboratory, the University of California at Santa Cruz, the University of Cambridge, Centro de Investigaciones Energeticas, Medioambientales y Tecnologicas-Madrid, the University of Chicago, University College London, the DES-Brazil Consortium, the University of Edinburgh, the Eidgenossische Technische Hochschule (ETH) Zurich, Fermi National Accelerator Laboratory, the University of Illinois at Urbana-Champaign, the Institut de Ciencies de l’Espai (IEEC/CSIC), the Institut de Fisica d’Altes Energies, Lawrence Berkeley National Laboratory, the Ludwig Maximilians Universitat Munchen and the associated Excellence Cluster Universe, the University of Michigan, NSF’s NOIRLab, the University of Nottingham, the Ohio State University, the University of Pennsylvania, the University of Portsmouth, SLAC National Accelerator Laboratory, Stanford University, the University of Sussex, and Texas A&M University.

BASS is a key project of the Telescope Access Program (TAP), which has been funded by the Na-

tional Astronomical Observatories of China, the Chinese Academy of Sciences (the Strategic Priority Research Program “The Emergence of Cosmological Structures” Grant #XDB09000000), and the Special Fund for Astronomy from the Ministry of Finance. The BASS is also supported by the External Cooperation Program of Chinese Academy of Sciences (Grant #114A11KYSB20160057), and Chinese National Natural Science Foundation (Grant #12120101003, #11433005).

The Legacy Survey team makes use of data products from the Near-Earth Object Wide-field Infrared Survey Explorer (NEOWISE), which is a project of the Jet Propulsion Laboratory/California Institute of Technology. NEOWISE is funded by the National Aeronautics and Space Administration.

The Legacy Surveys imaging of the DESI footprint is supported by the Director, Office of Science, Office of High Energy Physics of the U.S. Department of Energy under Contract No. DE-AC02-05CH1123, by the National Energy Research Scientific Computing Center, a DOE Office of Science User Facility under the same contract; and by the U.S. National Science Foundation, Division of Astronomical Sciences under Contract No. AST-0950945 to NOAO.

*Facilities:* Gemini:Gillett (GMOS longslit), Gemini:South (GMOS longslit)

*Software:* `extinction` (<https://extinction.readthedocs.io>), `IFSFIT` (Rupke 2014; Rupke et al. 2017), `ppxf` (Cappellari 2012, 2017), `PyPeIt` (Prochaska et al. 2020, 2023), `pyphot` (Fouesneau 2022), `speclite` (<http://dx.doi.org/10.5281/zenodo.8347108>), `WebPlot-Digitizer` (Rohatgi 2022)

## 6. APPENDIX INFORMATION

Here we display spectra of two stars and one un-IDed galaxy (Figure 6).

## REFERENCES

- Aird, J., Coil, A. L., & Georgakakis, A. 2019, MNRAS, 484, 4360, doi: [10.1093/mnras/stz125](https://doi.org/10.1093/mnras/stz125)
- Baldwin, J. A., Phillips, M. M., & Terlevich, R. 1981, PASP, 93, 5, doi: [10.1086/130766](https://doi.org/10.1086/130766)
- Balogh, M. L., Morris, S. L., Yee, H. K. C., Carlberg, R. G., & Ellingson, E. 1999, ApJ, 527, 54, doi: [10.1086/308056](https://doi.org/10.1086/308056)
- Best, P. N., & Heckman, T. M. 2012, MNRAS, 421, 1569, doi: [10.1111/j.1365-2966.2012.20414.x](https://doi.org/10.1111/j.1365-2966.2012.20414.x)
- Blakeslee, J. P., Jordán, A., Mei, S., et al. 2009, ApJ, 694, 556, doi: [10.1088/0004-637X/694/1/556](https://doi.org/10.1088/0004-637X/694/1/556)
- Bruzual, G., & Charlot, S. 2003, MNRAS, 344, 1000, doi: [10.1046/j.1365-8711.2003.06897.x](https://doi.org/10.1046/j.1365-8711.2003.06897.x)
- Byrne, C. M., & Stanway, E. R. 2023, MNRAS, 521, 4995, doi: [10.1093/mnras/stad832](https://doi.org/10.1093/mnras/stad832)
- Calzetti, D., Armus, L., Bohlin, R. C., et al. 2000, ApJ, 533, 682, doi: [10.1086/308692](https://doi.org/10.1086/308692)
- Cappellari, M. 2012, pPXF: Penalized Pixel-Fitting stellar kinematics extraction, Astrophysics Source Code Library, record ascl:1210.002. <http://ascl.net/1210.002>
- . 2017, MNRAS, 466, 798, doi: [10.1093/mnras/stw3020](https://doi.org/10.1093/mnras/stw3020)

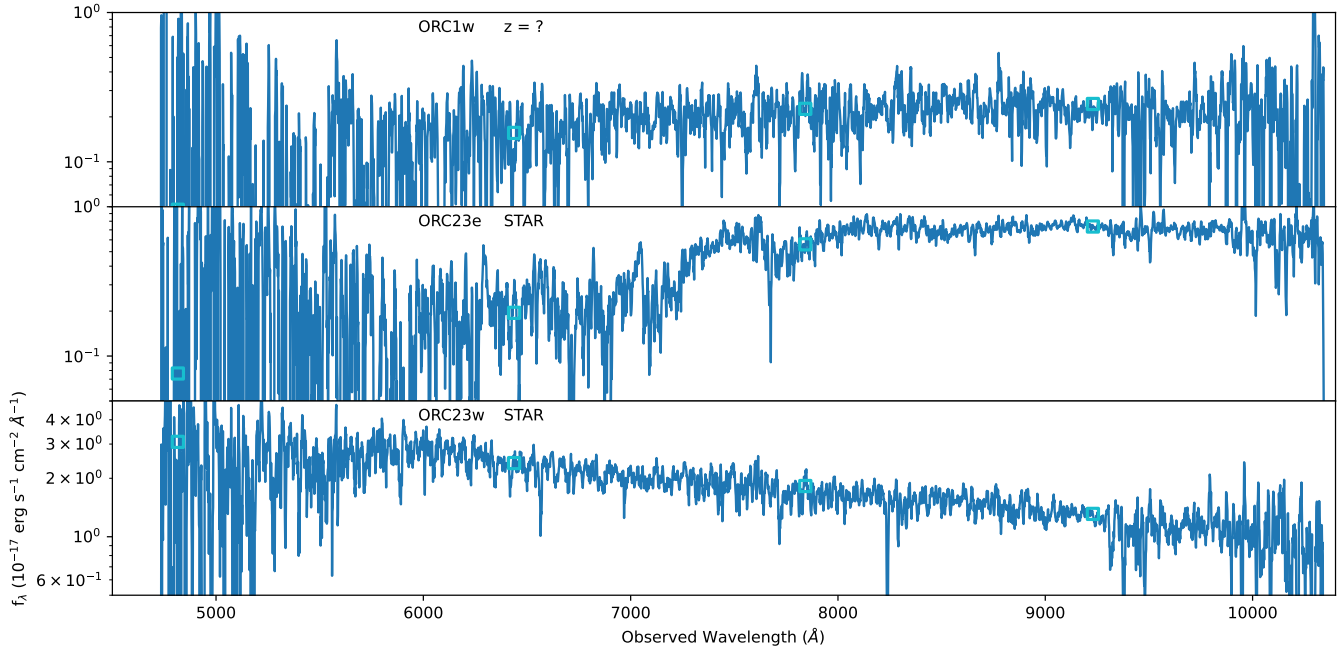


**Figure 6.** Observed-frame spectra of the unidentified source (ORC1w) and two stars (ORC23e/w).

- Cappellari, M., Bacon, R., Bureau, M., et al. 2006, MNRAS, 366, 1126, doi: [10.1111/j.1365-2966.2005.09981.x](https://doi.org/10.1111/j.1365-2966.2005.09981.x)
- Cardelli, J. A., Clayton, G. C., & Mathis, J. S. 1989, ApJ, 345, 245, doi: [10.1086/167900](https://doi.org/10.1086/167900)
- Choi, J., Dotter, A., Conroy, C., et al. 2016, ApJ, 823, 102, doi: [10.3847/0004-637X/823/2/102](https://doi.org/10.3847/0004-637X/823/2/102)
- Cid Fernandes, R., Stasińska, G., Schlickmann, M. S., et al. 2010, MNRAS, 403, 1036, doi: [10.1111/j.1365-2966.2009.16185.x](https://doi.org/10.1111/j.1365-2966.2009.16185.x)
- Cluver, M. E., Jarrett, T. H., Dale, D. A., et al. 2017, ApJ, 850, 68, doi: [10.3847/1538-4357/aa92c7](https://doi.org/10.3847/1538-4357/aa92c7)
- Coil, A. L., Perrotta, S., Rupke, D. S. N., et al. 2024, Nature, 625, 459, doi: [10.1038/s41586-023-06752-8](https://doi.org/10.1038/s41586-023-06752-8)
- Conroy, C., & Gunn, J. E. 2010, FSPS: Flexible Stellar Population Synthesis, Astrophysics Source Code Library, record ascl:1010.043. <http://ascl.net/1010.043>
- Conroy, C., Gunn, J. E., & White, M. 2009, ApJ, 699, 486, doi: [10.1088/0004-637X/699/1/486](https://doi.org/10.1088/0004-637X/699/1/486)
- Cutri, R. M., Wright, E. L., Conrow, T., et al. 2012, Explanatory Supplement to the WISE All-Sky Data Release Products, Explanatory Supplement to the WISE All-Sky Data Release Products
- Dey, A., Schlegel, D. J., Lang, D., et al. 2019, AJ, 157, 168, doi: [10.3847/1538-3881/ab089d](https://doi.org/10.3847/1538-3881/ab089d)
- Dolag, K., Böss, L. M., Koribalski, B. S., Steinwandel, U. P., & Valentini, M. 2023, ApJ, 945, 74, doi: [10.3847/1538-4357/acb5f5](https://doi.org/10.3847/1538-4357/acb5f5)
- Ekers, R. D., Goss, W. M., Wellington, K. J., et al. 1983, A&A, 127, 361
- Filipović, M. D., Payne, J. L., Alsaberi, R. Z. E., et al. 2022, MNRAS, 512, 265, doi: [10.1093/mnras/stac210](https://doi.org/10.1093/mnras/stac210)
- Foreman-Mackey, D., Hogg, D. W., Lang, D., & Goodman, J. 2013, PASP, 125, 306, doi: [10.1086/670067](https://doi.org/10.1086/670067)
- Fouesneau, M. 2022, pyphot, 1.4.3. <https://github.com/mfouesneau/pyphot>
- Gimeno, G., Roth, K., Chiboucas, K., et al. 2016, in Society of Photo-Optical Instrumentation Engineers (SPIE) Conference Series, Vol. 9908, Ground-based and Airborne Instrumentation for Astronomy VI, ed. C. J. Evans, L. Simard, & H. Takami, 99082S, doi: [10.1117/12.2233883](https://doi.org/10.1117/12.2233883)
- Gupta, N., Huynh, M., Norris, R. P., et al. 2022, PASA, 39, e051, doi: [10.1017/pasa.2022.44](https://doi.org/10.1017/pasa.2022.44)
- Heckman, T. M., & Best, P. N. 2014, ARA&A, 52, 589, doi: [10.1146/annurev-astro-081913-035722](https://doi.org/10.1146/annurev-astro-081913-035722)
- Ho, L. C. 2009, ApJ, 699, 626, doi: [10.1088/0004-637X/699/1/626](https://doi.org/10.1088/0004-637X/699/1/626)
- Hook, I. M., Jørgensen, I., Allington-Smith, J. R., et al. 2004, PASP, 116, 425, doi: [10.1086/383624](https://doi.org/10.1086/383624)
- Hotan, A. W., Bunton, J. D., Chippendale, A. P., et al. 2021, PASA, 38, e009, doi: [10.1017/pasa.2021.1](https://doi.org/10.1017/pasa.2021.1)
- Intema, H. T., Jagannathan, P., Mooley, K. P., & Frail, D. A. 2017, A&A, 598, A78, doi: [10.1051/0004-6361/201628536](https://doi.org/10.1051/0004-6361/201628536)
- Jarrett, T. H., Cluver, M. E., Brown, M. J. I., et al. 2019, ApJS, 245, 25, doi: [10.3847/1538-4365/ab521a](https://doi.org/10.3847/1538-4365/ab521a)

- Johnson, B. D., Leja, J., Conroy, C., & Speagle, J. S. 2021, *ApJS*, 254, 22, doi: [10.3847/1538-4365/abef67](https://doi.org/10.3847/1538-4365/abef67)
- Kauffmann, G., Heckman, T. M., White, S. D. M., et al. 2003a, *MNRAS*, 341, 33, doi: [10.1046/j.1365-8711.2003.06291.x](https://doi.org/10.1046/j.1365-8711.2003.06291.x)
- Kauffmann, G., Heckman, T. M., Tremonti, C., et al. 2003b, *MNRAS*, 346, 1055, doi: [10.1111/j.1365-2966.2003.07154.x](https://doi.org/10.1111/j.1365-2966.2003.07154.x)
- Kewley, L. J., Groves, B., Kauffmann, G., & Heckman, T. 2006, *MNRAS*, 372, 961, doi: [10.1111/j.1365-2966.2006.10859.x](https://doi.org/10.1111/j.1365-2966.2006.10859.x)
- Koribalski, B. S., Norris, R. P., Andernach, H., et al. 2021, *MNRAS*, 505, L11, doi: [10.1093/mnrasl/slab041](https://doi.org/10.1093/mnrasl/slab041)
- Kroupa, P. 2001, *MNRAS*, 322, 231, doi: [10.1046/j.1365-8711.2001.04022.x](https://doi.org/10.1046/j.1365-8711.2001.04022.x)
- Lamastra, A., Bianchi, S., Matt, G., et al. 2009, *A&A*, 504, 73, doi: [10.1051/0004-6361/200912023](https://doi.org/10.1051/0004-6361/200912023)
- Lang, D., Hogg, D. W., & Mykytyn, D. 2016a, The Tractor: Probabilistic astronomical source detection and measurement, *Astrophysics Source Code Library*, record ascl:1604.008. <http://ascl.net/1604.008>
- Lang, D., Hogg, D. W., & Schlegel, D. J. 2016b, *AJ*, 151, 36, doi: [10.3847/0004-6256/151/2/36](https://doi.org/10.3847/0004-6256/151/2/36)
- Lochner, M., Rudnick, L., Heywood, I., Knowles, K., & Shabala, S. S. 2023, *MNRAS*, 520, 1439, doi: [10.1093/mnras/stad074](https://doi.org/10.1093/mnras/stad074)
- Ma, X., Hopkins, P. F., Faucher-Giguère, C.-A., et al. 2016, *MNRAS*, 456, 2140, doi: [10.1093/mnras/stv2659](https://doi.org/10.1093/mnras/stv2659)
- Matthews, A. M., Condon, J. J., Cotton, W. D., & Mauch, T. 2021, *ApJ*, 914, 126, doi: [10.3847/1538-4357/abfaf6](https://doi.org/10.3847/1538-4357/abfaf6)
- McConnell, N. J., & Ma, C.-P. 2013, *ApJ*, 764, 184, doi: [10.1088/0004-637X/764/2/184](https://doi.org/10.1088/0004-637X/764/2/184)
- Molina, M., Eracleous, M., Barth, A. J., et al. 2018, *ApJ*, 864, 90, doi: [10.3847/1538-4357/aad5ed](https://doi.org/10.3847/1538-4357/aad5ed)
- Moustakas, J., Kennicutt, Robert C., J., & Tremonti, C. A. 2006, *ApJ*, 642, 775, doi: [10.1086/500964](https://doi.org/10.1086/500964)
- Moustakas, J., Lang, D., Dey, A., et al. 2023, *ApJS*, 269, 3, doi: [10.3847/1538-4365/acfaa2](https://doi.org/10.3847/1538-4365/acfaa2)
- Mullin, L. M., Riley, J. M., & Hardcastle, M. J. 2008, *MNRAS*, 390, 595, doi: [10.1111/j.1365-2966.2008.13534.x](https://doi.org/10.1111/j.1365-2966.2008.13534.x)
- Norris, R. P., Crawford, E., & Macgregor, P. 2021a, *Galaxies*, 9, 83, doi: [10.3390/galaxies9040083](https://doi.org/10.3390/galaxies9040083)
- Norris, R. P., Hopkins, A. M., Afonso, J., et al. 2011, *PASA*, 28, 215, doi: [10.1071/AS11021](https://doi.org/10.1071/AS11021)
- Norris, R. P., Intema, H. T., Kapińska, A. D., et al. 2021b, *PASA*, 38, e003, doi: [10.1017/pasa.2020.52](https://doi.org/10.1017/pasa.2020.52)
- Norris, R. P., Collier, J. D., Crocker, R. M., et al. 2022, *MNRAS*, 513, 1300, doi: [10.1093/mnras/stac701](https://doi.org/10.1093/mnras/stac701)
- Omar, A. 2022, *Research Notes of the American Astronomical Society*, 6, 100, doi: [10.3847/2515-5172/ac7044](https://doi.org/10.3847/2515-5172/ac7044)
- Pandya, V., Greene, J. E., Ma, C.-P., et al. 2017, *ApJ*, 837, 40, doi: [10.3847/1538-4357/aa5ebc](https://doi.org/10.3847/1538-4357/aa5ebc)
- Prochaska, J. X., Hennawi, J. F., Westfall, K. B., et al. 2020, *Journal of Open Source Software*, 5, 2308, doi: [10.21105/joss.02308](https://doi.org/10.21105/joss.02308)
- Prochaska, J. X., Hennawi, J., Cooke, R., et al. 2023, *pypeit/PypeIt: Version 1.12.0, 0.12.0*, Zenodo, doi: [10.5281/zenodo.7662288](https://doi.org/10.5281/zenodo.7662288)
- Rohatgi, A. 2022, *Webplotdigitizer: Version 4.6*. <https://automeris.io/WebPlotDigitizer>
- Rupke, D. S. N. 2014, *IFSFit: Spectral Fitting for Integral Field Spectrographs*, *Astrophysics Source Code Library*, record ascl:1409.005. <http://ascl.net/1409.005>
- Rupke, D. S. N., Gültekin, K., & Veilleux, S. 2017, *ApJ*, 850, 40, doi: [10.3847/1538-4357/aa94d1](https://doi.org/10.3847/1538-4357/aa94d1)
- Rupke, D. S. N., Coil, A., Geach, J. E., et al. 2019, *Nature*, 574, 643, doi: [10.1038/s41586-019-1686-1](https://doi.org/10.1038/s41586-019-1686-1)
- Rupke, D. S. N., Coil, A. L., Perrotta, S., et al. 2023, *ApJ*, 947, 33, doi: [10.3847/1538-4357/acbfae](https://doi.org/10.3847/1538-4357/acbfae)
- Salim, S., & Narayanan, D. 2020, *ARA&A*, 58, 529, doi: [10.1146/annurev-astro-032620-021933](https://doi.org/10.1146/annurev-astro-032620-021933)
- Sarbadhicary, S. K., Thompson, T. A., Lopez, L. A., & Mathur, S. 2022, *arXiv e-prints*, arXiv:2209.10554, doi: [10.48550/arXiv.2209.10554](https://doi.org/10.48550/arXiv.2209.10554)
- Sarzi, M., Falcón-Barroso, J., Davies, R. L., et al. 2006, *MNRAS*, 366, 1151, doi: [10.1111/j.1365-2966.2005.09839.x](https://doi.org/10.1111/j.1365-2966.2005.09839.x)
- Sarzi, M., Shields, J. C., Schawinski, K., et al. 2010, *MNRAS*, 402, 2187, doi: [10.1111/j.1365-2966.2009.16039.x](https://doi.org/10.1111/j.1365-2966.2009.16039.x)
- Schlafly, E. F., & Finkbeiner, D. P. 2011, *ApJ*, 737, 103, doi: [10.1088/0004-637X/737/2/103](https://doi.org/10.1088/0004-637X/737/2/103)
- Schweitzer, M., Lutz, D., Sturm, E., et al. 2006, *ApJ*, 649, 79, doi: [10.1086/506510](https://doi.org/10.1086/506510)
- Veilleux, S., & Osterbrock, D. E. 1987, *ApJS*, 63, 295, doi: [10.1086/191166](https://doi.org/10.1086/191166)
- Venturi, T., Rossetti, M., Brunetti, G., et al. 2017, *A&A*, 603, A125, doi: [10.1051/0004-6361/201630014](https://doi.org/10.1051/0004-6361/201630014)
- Yamasaki, S., Sarkar, K. C., & Li, Z. 2024, *MNRAS*, 528, 3854, doi: [10.1093/mnras/stae281](https://doi.org/10.1093/mnras/stae281)
- Yao, H. F. M., Jarrett, T. H., Cluver, M. E., et al. 2020, *ApJ*, 903, 91, doi: [10.3847/1538-4357/abba1a](https://doi.org/10.3847/1538-4357/abba1a)
- Yao, H. F. M., Cluver, M. E., Jarrett, T. H., et al. 2022, *ApJ*, 939, 26, doi: [10.3847/1538-4357/ac8790](https://doi.org/10.3847/1538-4357/ac8790)